The Dissertation Committee for André David Albert Certifies that this is the approved version of the following dissertation:

Nanostructured Ag Produced by LAMA

Committee:

Desiderio Kovar, Supervisor

Michael Becker

John Keto

Llewellyn Rabenberg

Paulo Ferreira

Nanostructured Ag Produced by LAMA

by

André David Albert, B.S.; M.S.E.

Dissertation

Presented to the Faculty of the Graduate School of

The University of Texas at Austin

in Partial Fulfillment

of the Requirements

for the Degree of

Doctor of Philosophy

The University of Texas at Austin

May 2007

Dedication

This dissertation is dedicated to my wife Sara, for her loving support.

Acknowledgements

There are many people who helped make this work possible. First and foremost is my advisor, Professor Desiderio Kovar, whose kind attention and sage advice were essential to both my research and my writing. I would also like to thank my co-advisors, Professors Michael Becker and John Keto for their expertise and input during this work. Drs. Paulo Ferreira and Steven Swinnea were invaluable with the TEM and XRD analysis contained in this dissertation.

I would also like to thank all my friends and colleagues for their support over the years I've spent at the University of Texas.

Nanostructured Ag Produced by LAMA

Publication No._____

André David Albert, Ph.D.

The University of Texas at Austin, 2007

Supervisor: Desiderio Kovar

The Laser Ablation of Microparticle Aerosol (LAMA) process is a technique for generating aerosolized nanoparticles (NPs) from a variety of starting materials. The NP aerosol produced from the LAMA process can be accelerated through a nozzle and impacted onto a substrate, with a deposition rate up to 60 mg/hour. This direct-write process can be used to create nanostructured lines or films up to hundreds of microns thick. NPs generated from the LAMA process are bare – they are not capped by an organic like NPs generated from chemical processes. This attribute may result in significantly lower processing temperatures for the written lines, even compared to other methods involving NPs produced by chemical processes (e.g., ink-jet printing). In this dissertation, we investigated the use of LAMA-produced Ag lines for bonding surfaces at low process temperatures (100 to 175°C). We studied the effects of process temperature and compression load on the strength of the Ag bonds, as well as the resistivity and the grain size of Ag deposits produced by LAMA. With these measurements and the use of known relationships between grain size and conductivity, we determined the effects of processing parameters on the final density of the Ag deposits. The strength and resistivity measurements compare favorably with similar work but at processing temperatures 50 to 100°C lower than previously achieved. The densification results agree qualitatively with established theory for pressure-assisted sintering.

Table of Contents

List of Tables

List of Figures

Chapter 1: *Introduction*

It is well known that properties of nanoparticles (NPs) can be significantly different than the properties of the same material in bulk form. For example, Ag NPs have been observed to melt at significantly lower temperatures than the melting temperature of bulk Ag.[1] Cu NPs have been observed to form necks and sinter at room temperature[2], and Ag NPs have been observed to coarsen at temperatures as low as 100°C.[3] Based on these properties, there has been interest in a variety of applications that exploit the depressed sintering temperatures of metallic NPs.

1.1 ELECTRICAL INTERCONNECTS

One area of interest involves the use of NP-based inks for ink-jet printing of electrically conductive interconnects[4-8]. There are a variety of applications for patterned metallic conductors, including hybrid circuits, microcircuits, and displays. These conductors are conventionally prepared through the use of microparticle-based pastes, which are deposited onto the substrate, allowed to dry, and subsequently heated to improve conductivity through pyrolysis and then sintering. To achieve acceptable conductivities, the sintering temperature of the microparticle-based pastes must be in the range of 700-900°C[9]. This limits the choice of substrates to those that can withstand these processing temperatures, such as glass and ceramic substrates. Switching to NP-based inks allows the sintering temperature to be reduced to approximately 300°C[5,6,8].

However, the sintering of NP-based inks is inhibited by the presence of organics added to the inks in order to prevent agglomeration of the NPs. These organics must be removed from the ink before the NPs can sinter, which requires a minimum processing temperature of around 280°C[5,8,10].

Another approach to writing conductive lines at low process temperatures utilizes a Au NP ink that is printed on a substrate that is heated to 90°C. The printed ink is cured by a pulsed laser in tandem with the printing process. The reported resistivities from this approach are 3-4 times the resistivity of bulk Au[11-15].

1.2 DEVICE INTERCONNECTS AND DIE ATTACH METHODS

Another application where nanocrystalline Ag has been studied is for the replacement of solders as a die attach method or a device interconnect. The strength of the metal/substrate interface and the interparticle bonding are important criteria in these applications. Thus, for these applications, pressure has been utilized to produce strong bonds while further reducing the processing temperatures required. For example, Schwarzbauer and Kunhert reported the use of a Ag-based paste to join metallized Si substrates to Mo disks for power device applications[16]. Their devices had reported shear strengths of 100 MPa after being processed at 40 MPa and around 220°C. More recently, there has been interest in the use of Ag NPs as a power device interconnect material[10,17-20]. Ag NP-based techniques offer many attractive properties for this type of application: high electrical and thermal conductivity, good thermomechanical reliability, low processing temperatures, and high melting temperatures. Research in this area has been

conducted both with[18] and without[10,17,19,20] pressure applied during the sintering process. Pressure-assisted sintering conducted at 40 MPa at a temperature of 240°C resulted in Ag joints with a reported shear strength of 50 MPa and a resistivity of 2.4 μΩ cm,[18] a resistivity of less than twice the value of bulk Ag (1.63 μΩ cm).[21] Regarding techniques not involving pressure, Bai et al. reported the use of pastes containing 30 nm Ag NPs that resulted in a resistivity of 3.8 μΩ cm after being sintered at 280°C for 10 minutes. The Ag joints on Au metallized substrates from this process exhibited shear strengths of about 21 MPa[10,20].

1.3 TEMPERATURE SENSITIVE MEMS DEVICES

Temperature sensitive MEMS devices are currently sealed through the use of low melting temperature solder or braze materials. Low reflow temperature solders, such as lead-tin (214°C), result in seals with low shear strengths (27 MPa)[10]. Other solder compositions, such as gold-tin, can be used for higher strength seals, but these compositions also have higher reflow temperatures (320°C). For MEMS devices that are sensitive to temperatures in this range, a lower-temperature, high-strength, hermetic sealing process would be desirable.

1.4 CHALLENGES FOR DIRECT WRITING OF METALLIC LINES AT LOW PROCESS TEMPERATURES

While there has been interest in exploiting the depressed sintering temperatures of Ag NPs for a variety of technologically important applications, the proposed techniques have all involved NPs with organic coatings required to prevent agglomeration. These organic coatings interfere with sintering processes until they are pyrolyzed at temperatures in the range of 280°C or higher. The relevant properties (electrical conductivity, thermal conductivity, strength) of the NP-based deposits are all strongly affected by the density of the deposit, and could therefore be improved by further densification of the deposits. Since there is evidence that NPs can sinter and densify at temperatures lower than 280°C, the processing temperatures required for these applications could be further reduced if a technique that did not require organics to prevent agglomeration of the NPs could be utilized. The use of pressure during the sintering process is also expected to further depress the temperatures required as well as inhibit grain growth, which would improve the strength of the deposit[22].

One approach to directly writing patterned lines without the use of organics was developed by Hayashi and colleagues[23-26]. Their Gas Deposition Method (GDM) involves evaporation from a hot source, which creates an aerosol of metal NPs with a mean size of 60-100 nm in a pressure of 13-10 kPa. The deposition chamber is pumped down to a pressure of less than 1.3 mPa, resulting in a pressure difference that causes the aerosol to be accelerated through a nozzle and impacted onto a movable substrate. The impaction velocities are sufficient for the NPs to deposit into films. When using argon as

a carrier gas, Ni films produced using this method had about two orders of magnitude higher resistivity in the as-deposited state than the corresponding bulk material[24]. This work demonstrated the potential for an aerosol process to produce high density patterned films at low process temperatures, but there is room for a significant amount of scientific advancement regarding the effects of the NP generation method. For example, the effect of particle size on the deposition density and resultant film properties was not established. It is also unclear whether the NPs in this method agglomerate during the process, since there is no method for preventing agglomeration inherent to the process. The agglomeration of the NPs during the process could affect the density of the deposit and therefore the resulting properties of the films. Subsequent processing of the films was also not initially considered: the influence of annealing temperature on film microstructure and properties was not studied.

The Laser Ablation of Microparticle Aerosol (LAMA) process is a method for producing a NP aerosol from a variety of starting materials, including metals, glasses, and semiconductors at high volumetric rates[27-34]. The NP size can be controlled from about 2 to 40 nm by varying processing parameters. The created NP aerosol is accelerated through a nozzle and deposited onto a translating substrate, making the LAMA technique a serial additive (direct-write) process. NPs produced by the LAMA process are charged by the ablation process and therefore do not require an organic surfactant to prevent agglomeration. The lack of a capping agent and the very fine NP size that can be achieved by LAMA could allow nanostructured Ag lines produced by the LAMA process to densify and sinter either during deposition or at low post-processing temperatures. The addition of pressure during the heat treatment should further improve the low temperature

sinterability of nanocrystalline lines. Densification is expected to improve a number of material properties, including strength and both electrical and thermal conductivity.

As the NPs generated through LAMA are not capped by an organic, the use of the LAMA technique provides a unique opportunity to study the low-temperature densification of NPs without the interference of surfactants or other organics. We have studied the effects of multiple processing parameters in an effort to both understand the densification of nanostructured Ag as well as its suitability as a solder replacement for temperature sensitive MEMS devices. This includes the effects of temperature, compressive load, and deposit thickness on the bond strength of nanostructured Ag deposited on metallized wafers. We also studied both the conductivity and the grain size of the Ag after processing, in order to understand the effects of temperature and compressive load on grain size and density of the nanostructured Ag films. The results of our research are presented here and discussed with respect to similar work. Conclusions based on our research are drawn, and possible future work in this area is outlined.

Chapter 2: *Background*

This chapter covers general background information useful for understanding the research in subsequent chapters. The dependence of both strength and conductivity on density and grain size is explained, justifying an interest in densification of the Ag deposits. A brief background on sintering is presented, explaining the motivations behind the processing of the samples.

2.1 FACTORS THAT INFLUENCE STRENGTH

There are two main parameters that influence the strength of porous, nanocrystalline materials such as the deposits investigated in this study: grain size and density. For poly-crystalline materials, the Hall-Petch relationship[35,36] predicts that yield strength increases with decreasing grain size:

$$\sigma = \sigma_0 + kd^{-1/2} \quad \textbf{(1)}$$

where σ is the yield stress and d is the average grain size. σ_0 is usually rationalized as either a frictional stress resisting gliding dislocation motion or an internal back stress. k is the Hall-Petch slope, which is considered a measure of the grain boundary's resistance to slip transfer.

The Hall-Petch relationship also holds for the grain-size dependence of hardness:

$$H = H_0 + k_H d^{-1/2} \quad \textbf{(2)}$$

where H, H_0, and k_H correlate to the similar terms from Eq. (1). It is worth pointing out that Vickers hardness can be correlated to yield strength with the following relation:

$$H_V \approx 2.8 Y_R \quad \textbf{(3)}$$

where H_v is the Vickers hardness and Y_R is the flow stress in simple compression at a strain of about 0.08.[37] This relationship allows us to predict the yield strength of our Ag deposits based on grain size.

While there has been some debate about whether or not the Hall-Petch effect holds for nanoscale materials,[38-40] Qin et al. have studied the effects of grain size and density on the hardness of nanostructured Ag compacts.[41] For the studied size range of 17-105 nm, they found that a normal Hall-Petch relation holds for Ag. Therefore, the smaller the grain size of our Ag deposits, the higher the expected strength.

For porous materials, density has a significant effect on the strength of the material.[42] The strength dependence on density can be empirically represented as:

$$R_m = R_{m,0}(1-P)^n \quad \textbf{(4)}$$

where R_m is the tensile strength of the porous material, $R_{m,0}$ is the tensile strength of the fully dense material, P is the fractional porosity, and n is a value from 3 to 6 that is affected by pore shape.[42] It is also worth noting that the ductility is very limited at porosities higher than 15%, which means that the tensile strengths and the yield strengths of our deposits are essentially equivalent.[42]

2.2 FACTORS THAT INFLUENCE RESISTIVITY

From Matthiessen's rule, the resistivity of a film can be written as:

$$\rho' = \rho_{ph} + \rho_D + \rho_S + \rho_{gb} \quad \textbf{(5)}$$

where ρ' is the resistivity of the film, and ρ_{ph}, ρ_D, ρ_S, and ρ_{gb} represent the contributions to the resistivity from phonon, defect/impurity, surface, and grain boundary scattering, respectively.

Electron-phonon scattering is an intrinsic material property affected only by temperature changes, and therefore ρ_{ph} for our films is expected to be similar to the bulk value.[43]

While defects and impurities increase the resistivity of films, there is no evidence of significant defects or impurities in our films. Based on previous TEM and XRD analysis,[44] the NPs of our films are not heavily defective, other than twinning in the larger particles. The LAMA process is also an intrinsic high-purity process, therefore scattering due to defects or impurities can be neglected.

For our films, the small surface/volume ratio of the samples we studied renders surface scattering negligible. Previous analysis using a modified Fuchs-Sondheimer equation showed that ρ_S is expected to be less than 1% of ρ'.[45] Hence, surface scattering can also be neglected for our Ag deposits.

Grain size has a strong effect on resistivity of Ag when the grain size approaches the mean free path length of electrons, and therefore must be considered when modeling the resistivity of our deposits. Density of a film also has an effect on resistivity. Mathiessen's rule does not include a density term, so for our films, a density term, ρ_d, must also be considered. Fortunately, the effects of density and grain size on the resistivity of nanostructured Ag have already been studied by Qin et al.[46]

Qin's model relates grain size to conductivity through the following equation:

$$T^* = e^{\lambda / d} \ln\left(\frac{\rho}{\rho_{bulk}}\right) \quad \textbf{(6)}$$

where T*, λ, d, ρ, and ρ_{bulk} represent Qin's electron transmission coefficient T*, mean free path λ, grain size d, resistivity of the nanostructured Ag ρ, and bulk resistivity ρ_{bulk}.

This analysis was based on two observations. Reiss et al. previously modeled electrical conductivity by considering electron motion through boundaries with an electron transmission T*.[47] Electrons trapped at the boundaries are removed from the conduction process, giving the $T^{*(-\lambda/d)}$ relation to resistivity. Schaefer et al. used positron spectroscopy to show that electron scattering at boundaries in nanocrystalline Fe is completely specified by density.[48] Therefore, Ag samples with the same density have the same T*. Qin et al. experimentally determined a linear relationship between ln(T*) and 1/D, where D is the fractional density of the nanostructured Ag film. Qin et al. also used their experimental results to quantify the electron mean free path for Ag samples with grain sizes smaller than 45 nm, where mean free path is no longer constant with respect to grain size. By using these results and measuring both the resistivity and grain size of a nanostructured Ag film, the density of the film can be determined.

2.3 SINTERING

Solid-state sintering involves mass transport from regions of high chemical potential to regions of low chemical potential. For polycrystalline materials, there are multiple paths or mechanisms by which this can occur. These mechanisms can be divided into two categories: mechanisms that result in densification, and mechanisms that result in coarsening. These differing mechanisms are represented schematically in Figure 1.

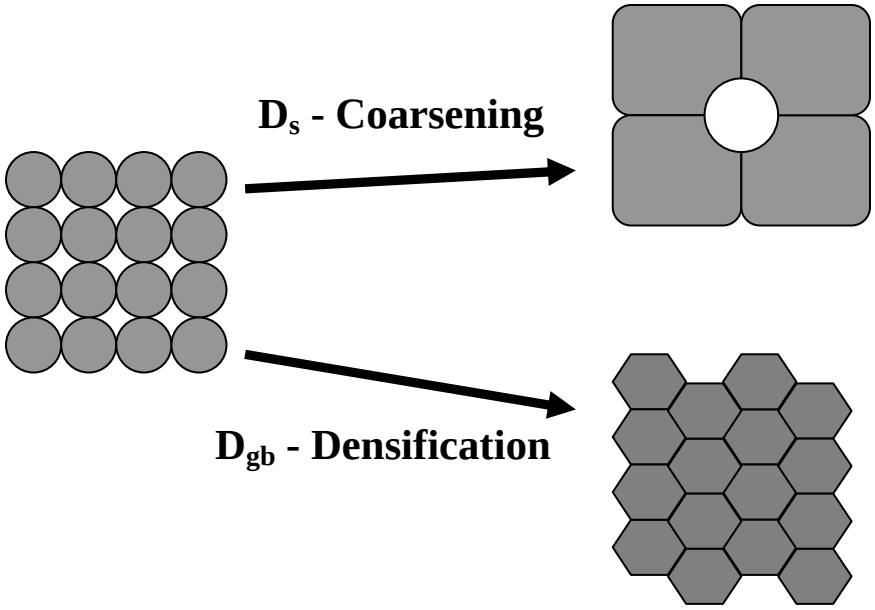

Figure 1. Comparison of densification and coarsening.

Mass transport through along the grain boundary (grain boundary diffusion) results in densification whereas both vapor phase transport by evaporation/condensation and surface transport result in coarsening. Mass transport through the lattice (lattice

diffusion) results in both densification and coarsening. Since densification and coarsening rely on the same driving force to occur, it is important to limit coarsening if high densities are desired.

Sintering models are separated into three stages, based on the density of the sample. The final sintering stage begins when pores are no longer interconnected and have reached an equilibrium shape, which typically occurs at densities of around 90%. The idealized model for this sintering stage considers the grains as tetrakaidecahedra with spherical, monosize pores located at corners.

One way to consider whether a process will result in densification or coarsening is to compare the densification and coarsening rates as a ratio. This ratio can be expressed as a dimensionless parameter Γ, in the form[22,49]

$$\Gamma = \frac{3}{176}\frac{\delta_s}{\delta_{gb}}\frac{D_s}{D_{gb}}\frac{\gamma_{gb}}{\gamma_s} \quad \textbf{(7)}$$

where δ_s is the effective surface depth,[50] δ_{gb} is the grain boundary width,[50] D_s is the surface diffusivity,[51] D_{gb} is the grain boundary diffusivity,[51] γ_{gb} is the grain boundary energy,[52] and γ_{sv} is the specific surface energy.[53] For this expression, a Γ of less than 1 corresponds to a regime where densification dominates, and a Γ of greater than 1 corresponds to a regime where coarsening dominates. Although this model only considers surface and grain boundary diffusion, it is valid for our work because lattice

diffusion is predicted to be insignificant compared to surface and grain boundary diffusivities for nanomaterials at our temperatures of interest.

The application of pressure during the sintering process can significantly increase the driving force for densification. For example, materials such as Si_3N_4 and SiC that cannot be densified by pressureless sintering, are easily densified by pressure-assisted sintering.[54] Based on the creep equations developed by Coble,[55] an approximation of the densification rate can be expressed as:

$$\frac{1}{D}\frac{dD}{dt} = \frac{15}{2}\left(\frac{D_{gb}\delta_{gb}\Omega}{d^3 kT}\right)\left(p_a\phi + \frac{2\gamma_{sv}}{r}\right) \quad \textbf{(8)}$$

where D is the relative density, D_{gb} is the grain boundary diffusion coefficient, δ_{gb} is the grain boundary width, Ω is the atomic volume, d is the grain size, k is Boltzmann's constant, T is absolute temperature, p_a is the applied stress, ϕ is the stress intensification factor, γ_{sv} is specific surface energy, and r is the pore radius. This is a final stage sintering model, where grain boundary diffusion is the dominant mechanism.[22]

From the discussion in the preceding sections of this chapter it is apparent that if a porous, nanocrystalline metal were densified, the strength and conductivity would increase since the contact area between the particles would increase (beneficial for both strength and conductivity) while retaining a fine grain size (beneficial for strength). Conversely, there are competing effects that determine how strength would be influenced by coarsening. The increase in contact area between particles that occurs during

coarsening should result in increased strength whereas the increase in grain size would be expected to be detrimental to strength. Coarsening, however, would be beneficial to conductivity since the increase in neck area and the increase in grain size would both reduce scattering.

Chapter 3: *Experimental Procedures*

3.1 DEPOSITION PROCEDURE

A schematic of the LAMA process used to write nanostructured Ag lines onto metallized Si substrates is shown in Figure 2.

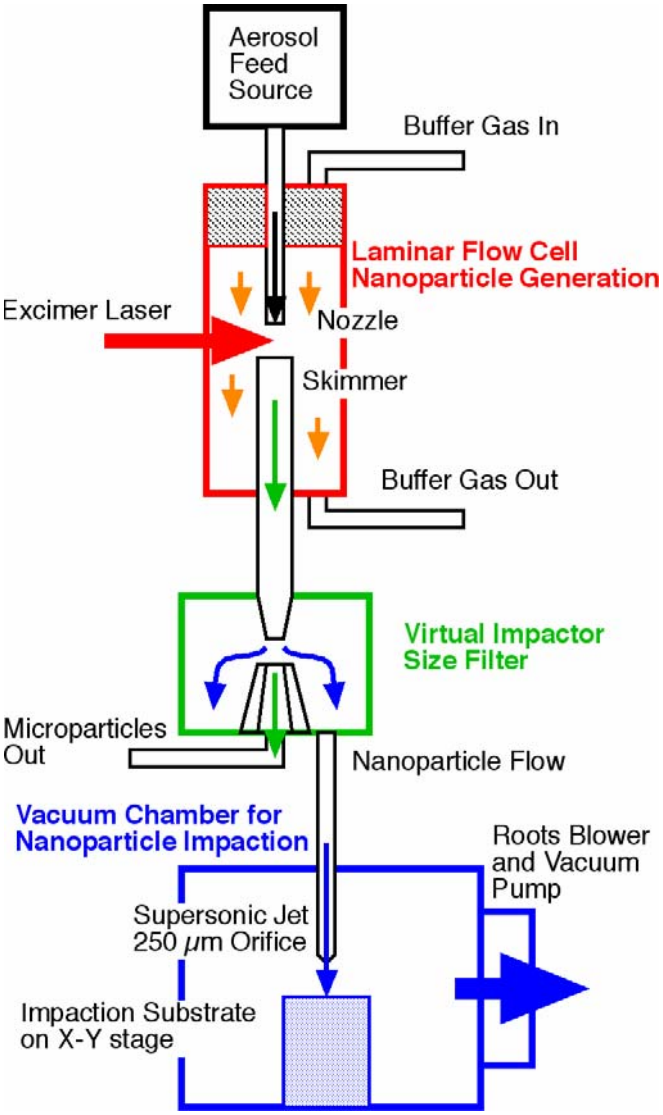

Figure 2. Schematic of the LAMA process[33].

The feedstock consisted of a conventional, commercially available, silver powder with a mean particle diameter of 2 μm. This powder was aerosolized in a fluidized bed feeder using He (99.99% pure) as the carrier gas. The flow rate of the He through the powder feeder was 110 standard cm^3/min. This aerosol comprised the center flow portion of the gas input to the LAMA system. In order to maintain laminar flow through the ablation region, a buffer gas (also He, same purity) was fed into the system at a linear velocity equal to the center flow velocity (3700 standard cm^3/min), providing a sheath to the center flow. The aerosol exited the ablation nozzle (cross-sectional area of 4.6 mm^2) where it was irradiated by a high energy excimer laser focused to a fluence of 1.2 - 2.0 J/cm^2. The linear velocity of the aerosol at the ablation nozzle exit was 40 cm/sec. The height of the beam at focus in the ablation region was 4 mm, and the laser repetition rate was set to 200 Hz. The repetition rate of the laser was set so that each plug of aerosol (a section of aerosol volume equal to the volume of aerosol illuminated by the laser) was irradiated twice, thereby limiting the population of unablated microparticles that remained in the aerosol.

The laser pulse initiated breakdown and a shockwave at each microparticle[32]. Spherical NPs nucleated and coalesced out of the plasma generated by the breakdown of the microparticles. The size of the NPs produced depends on both the carrier gas used and the pressure in the ablation cell[29]; the processing conditions used in these experiments resulted in an average particle size of 6 nm[34]. As produced, the NPs are charged due to both photoionization and thermionic emission, preventing agglomeration for the period of time that the particles remain charged[29].

After the ablation region, the aerosol passed by a virtual impactor, which removed remaining microparticles from the aerosol. Particles of diameter greater than 500 nm do not stay entrained in the aerosol at the bend over the virtual impactor and are removed from the system in this region.[29] Particles of a diameter less than the cut-off size stay entrained in the aerosol throughout the virtual impactor region and continue on to the deposition chamber.

While both the ablation cell and virtual impactor were at atmospheric pressure (760 Torr), a deposition chamber pressure of 250 mTorr was maintained during deposition. This pressure differential accelerated the NP aerosol through the deposition nozzle and caused the NPs to impact the substrate at high velocity. The density and grain size of a deposited line depends on the impact velocity of the NPs, which in turn depends on a variety of process parameters, including the carrier gas, nozzle geometry and NP size. The width of a deposited line depends on both the nozzle geometry and nozzle-to-substrate distance. For these experiments, a flat-plate nozzle was used, where both the diameter and the length of the orifice were 250 μm. The width of the deposited line depends on the distance from the deposition nozzle to the substrate. For these experiments, that distance was held constant at 1 mm. The nozzle to substrate distance was set using a spacer with a thickness equal to the thickness of the substrate plus the desired nozzle-to-substrate distance. The spacer was placed on the sample stage and the deposition nozzle was adjusted so that it just contacted the surface of the spacer. The spacer was then removed, leaving the desired gap between the deposition nozzle and the substrate on the sample stage.

Patterns of lines or films were produced by moving the substrate with respect to the deposition nozzle by means of a computer controlled x-y stage. For these experiments, two types of deposition patterns were used, square and serpentine. For strength testing, a 5 mm per side square pattern was used on metallized substrates (Figure 3). Each square pattern was written with 10, 20, or 30 directly overlapping passes to vary the thickness of the resulting deposit.

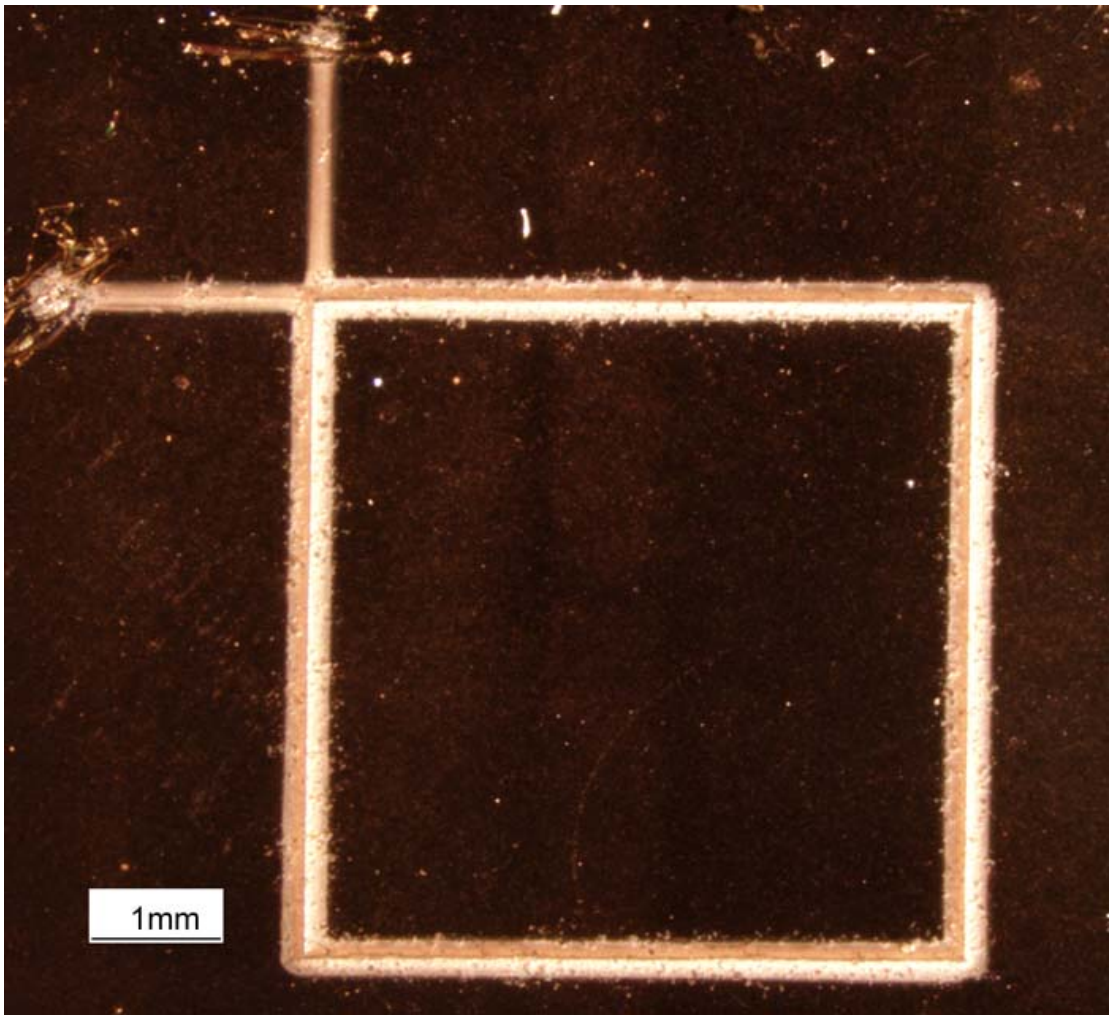

Figure 3. Optical micrograph plan view of patterned Ag line.

To prevent deposition buildup at the beginning and end of the run, the line pattern contained a single pass outside of the square for both the start and stop position of the substrate (upper left-hand corner, Figure 3). The resulting deposit in this region was not thick enough to contribute to bonding during subsequent processing.

For the conductivity and XRD analysis, a serpentine pattern with a long side length of 1 cm was deposited onto a glass substrate (Figure 4).

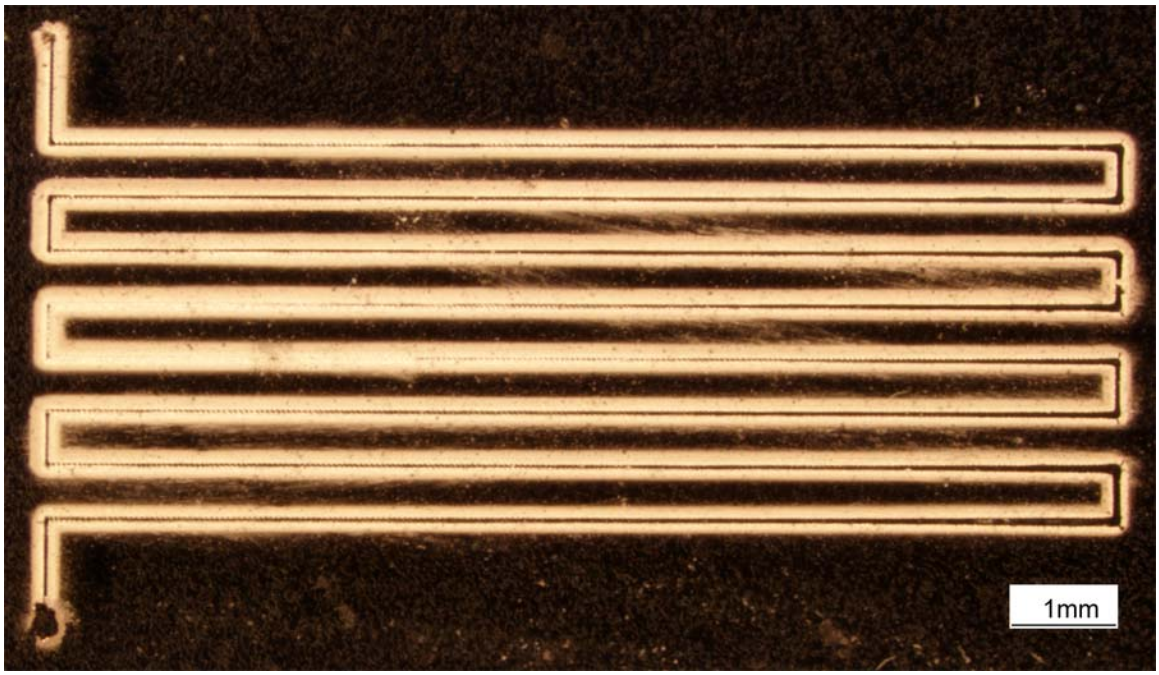

Figure 4. Optical micrograph plan view of a serpentine pattern after compression. The dark centerline is the flat topped region developed during compression.

All serpentine patterns were deposited with 15 overlapping passes in an effort to minimize thickness variations from sample to sample. The legs at the beginning and end

of the serpentine pattern represent the start and stop points of the pattern, and deposit build-up at these points was removed by scratching this portion of the line off the substrate using a razor blade prior to any compression of the samples. The linear speed of the motor stage was approximately 1.4 mm/sec. Thus, a 30 pass, square pattern sample was written in about 8 minutes, whereas a serpentine pattern required 15 minutes to deposit.

The metallized substrates used to prepare samples for strength testing were Si wafers coated by evaporation with a 50 nm thick layer of Cr followed by a 110 nm thick layer of Au. All substrate surfaces were cleaned with ethanol prior to deposition. These metallization layers were chosen to enable comparison with previous work and also because they were expected to result in well-adhered metal coatings on the wafers. The serpentine patterns were deposited onto standard microscope slide glass, also cleaned with ethanol prior to deposition.

3.2 PROFILOMETRY PROCEDURE

After deposition, a Dektak3 stylus profilometer was used to profile the cross-section of the deposited lines. For the square pattern samples, one scan was performed across each of the four sides of each sample (Figure 5). The white lines indicate the approximate locations of the scan paths.

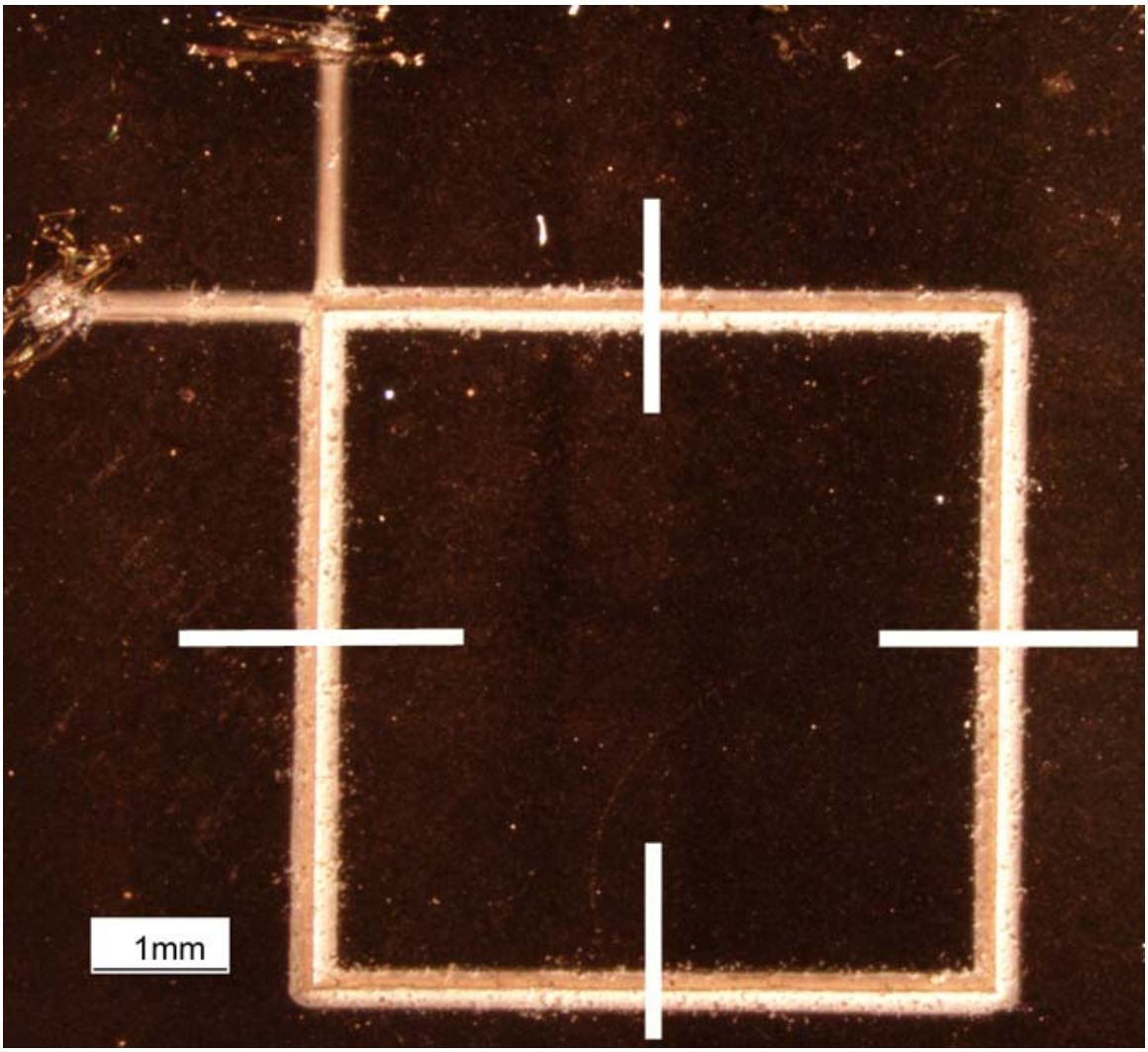

Figure 5. Typical profilometer scan paths for a square sample.

These scans were used to calculate the average height of the square sample as deposited. The scan distance was 1.25 mm and took 31 s to complete. The thicknesses of the square samples varied from 16.5 to 154 μm, with most samples in the 30 - 100 μm range.

For the serpentine pattern samples, two preliminary scans were performed on all the samples in order to gauge the as-deposited thicknesses of the samples. These two scans were taken across all 8 long segments, with one scan at each end of the sample (Figure 6).

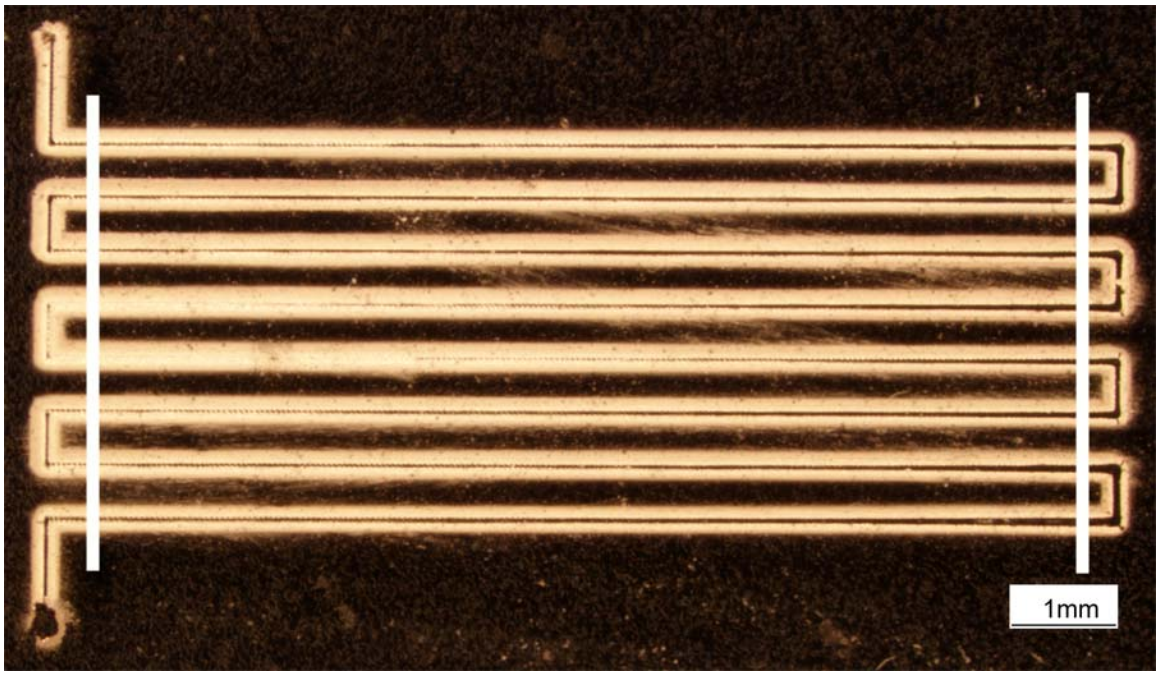

Figure 6. Typical profilometer scan paths for a serpentine sample.

Again, the white lines indicate typical scan paths. For these scans, the travel distance was set to 4.5 mm, with each scan taking 44 s to complete. After processing of the samples and performing conductivity measurements, additional profiles were measured in order to calculate the cross-sectional area of the lines of interest. Five scans were conducted at approximately equal spacings across each line, with a travel distance of 1 mm and a scan time of 50 s.

For all samples, the profilometer was set to the 2 mm height range and run at the low scan speed. The resolution of the scan depends on the travel distance used, the 1 mm, 1.25 mm and 4.5 mm scan lengths had resolutions of 0.5, 1, and 2.5 μm. The stylus used had a diamond tip with a radius of 12.5 μm, and the stylus force was set to 10 mg in order to prevent damage to the deposited lines.

3.3 COMPRESSION PROCEDURE

After deposition of the Ag line patterns, the square pattern samples were compressed at low temperature and moderate pressure in order to densify the lines (Figure 7).

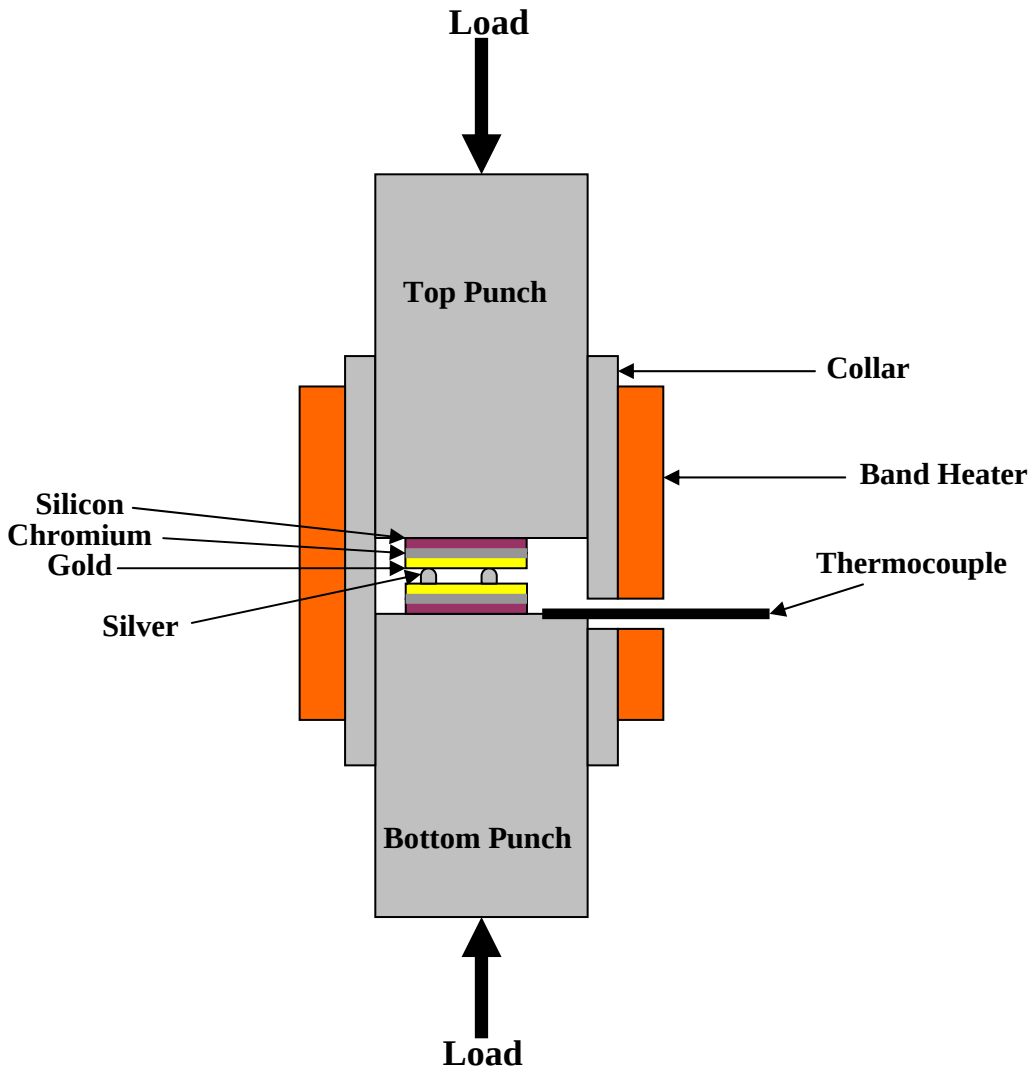

Figure 7. Cross-section of the bonding process.

The location of the line pattern with respect to the substrate was indicated on the underside of the deposition substrate through the use of a marker before compression. These markings allowed for alignment of the sample during subsequent tension testing.

To bond the substrates, the system was first allowed to reach the desired sealing temperature, after which the deposition substrate was placed onto the bottom punch. A blank metallized Si substrate was placed face down on top of the deposition substrate. The top punch was then placed in the collar and a small preload (~10 N) was applied to the sample while the temperature equilibrated (3-15 minutes). The collar kept the surfaces of the punches parallel, allowing the sample to be loaded in a uniform manner. After the equilibration period, the sample was compressed at a rate of 0.15 mm/min to the desired load, a process that took at most 2 minutes. The maximum load that could be applied to the samples was dictated by fracture of the substrates; loads greater than about 600 N caused the Si substrates to fracture. Due to thermal expansion of the test frame during the compression of the samples, if the displacement was held constant, the load on the sample would increase significantly during testing. Therefore the load was cycled just above and below the desired load point (±10 N), allowing the displacement-controlled test frame to run in pseudo-load control. Each sample was kept under load at the desired temperature for 1 hour. The substrate was heated by a 150 W band heater attached directly to the collar. The temperature was measured with a type K thermocouple threaded through a hole in the collar, with the tip at the height of the deposition substrate and only millimeters away from the substrate. An Omega CN9000A controller was auto-tuned for the test fixture and used to control the sample temperature.

A 10 kN load cell was used for compression of the samples, giving a resolution of about ±1 N.

The serpentine pattern samples were compressed in a similar fashion with the same equipment, except that it was desirable for there to be no bonding to the top substrate to allow for subsequent conductivity and XRD analysis. Therefore, the blank substrate was an uncleaned piece of glass for the serpentine samples. This prevented bonding during the compression of the samples.

3.4 TENSION TESTING PROCEDURE

After the bonding process, the samples with the square deposition pattern were prepared for tension testing (Figure 8).

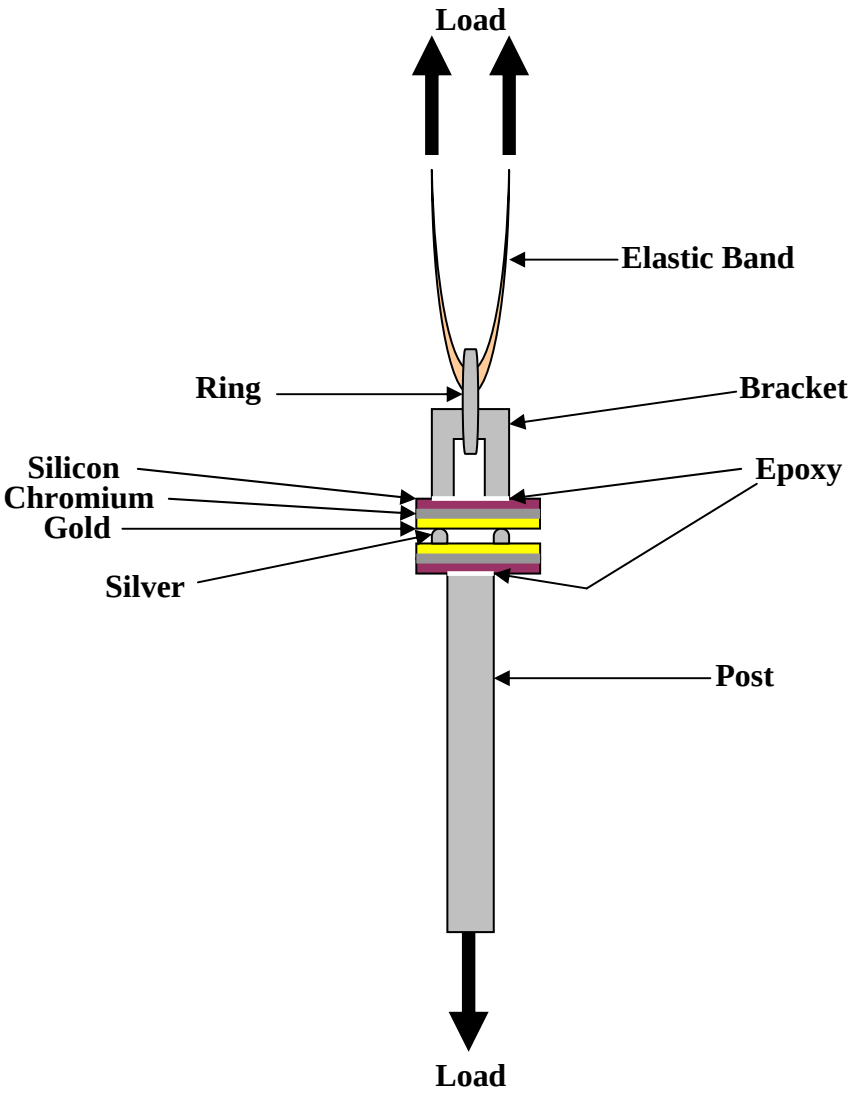

Figure 8. Schematic of tension testing procedure.

A ¼ inch (6.35 mm) diameter cylindrical post was bonded using Devcon High Strength 2 Ton White Epoxy (product number S-30 30345) to the deposition substrate side of each square pattern sample and aligned with the line pattern using the markings made at the beginning of the sealing process.

A bracket was bonded using the same high strength epoxy to the top substrate side of each square pattern sample. The channel in the bracket was 1/8 of an inch wide (3.2 mm), allowing a ring to be inserted to carry the tensile load. A 5/8 inch (15.9 mm) diameter ring was used to connect an elastic band to the bracket. Using a ring and elastic band in this manner allowed the sample to be smoothly loaded from zero load (important for low strength samples) and helped ensure the application of a uniaxial load on the sample by eliminating moment and shear carrying elements of the sample. The sample was tested at a displacement rate of 50 mm/min until failure, with a typical test taking about 10 minutes. A 250 N load cell was used for tension testing, giving a resolution of ±0.025 N.

3.5 FRACTURE AREA MEASUREMENT PROCEDURE

After failure of the sample during the tension test, optical microscopy was used to measure the width of the bonded region of the deposit. The entire perimeter of each sample was observed in an optical microscope in order to accurately assess the average line width of each sample.

Figure 9 shows a typical image of a line after testing. The in-focus region with bright contrast in the upper left shows debonded Au/Cr from the top substrate. The vertical strip of material in focus at the same plane shows the fracture surface of the visible segment of deposited line.

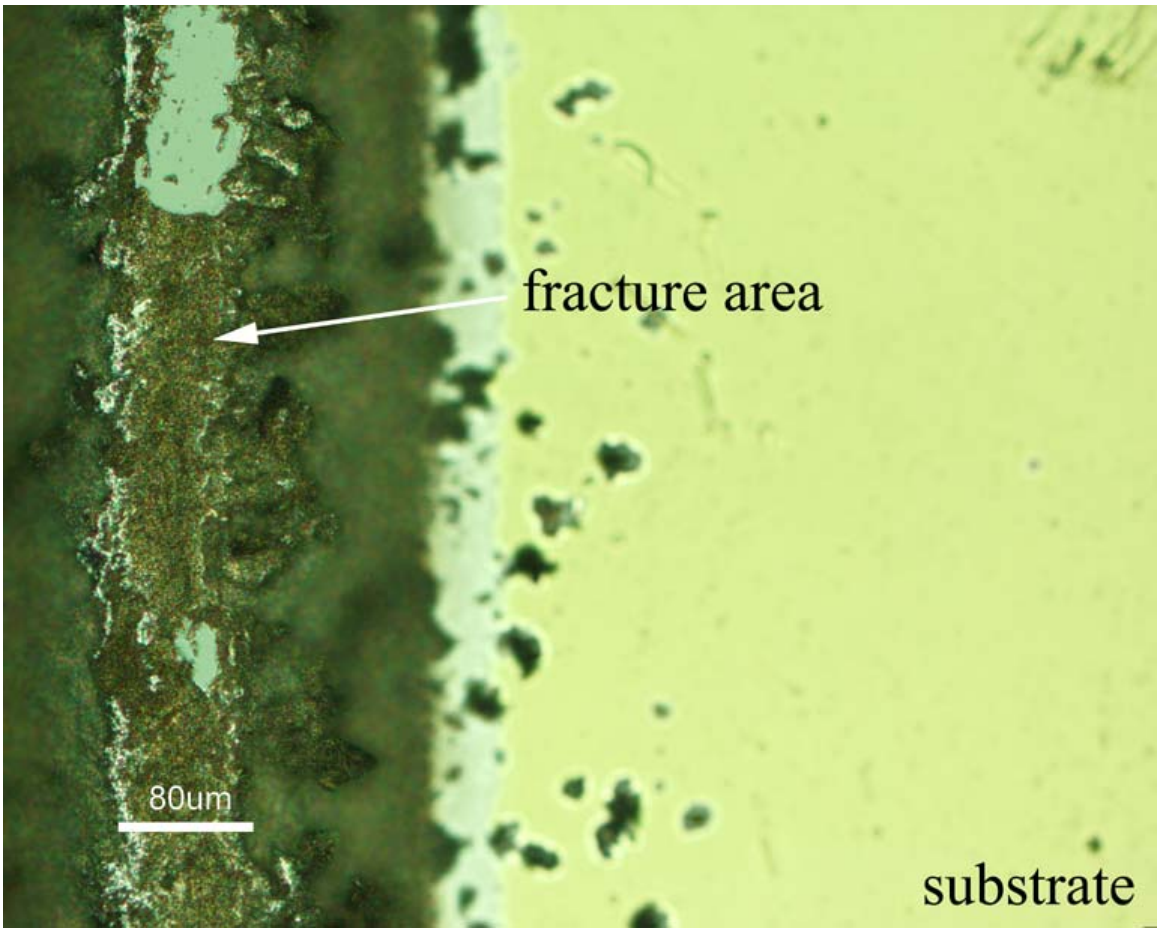

Figure 9. Optical micrograph showing the line width of a sample after fracture.

This line width was used for two calculations. The tensile strength of each sample was calculated based on the load at failure and the sample area. The sample area was taken to be the product of the line length (20 mm for the square samples) and the average line width. This sample area was also used to estimate the mean compressive stress imposed on each sample during bonding.

3.6 CONDUCTIVITY

The conductivity of the serpentine samples was analyzed using a four-point probe method using the same procedure described in earlier work.[44] A schematic of the experimental set-up is shown in Figure 10.

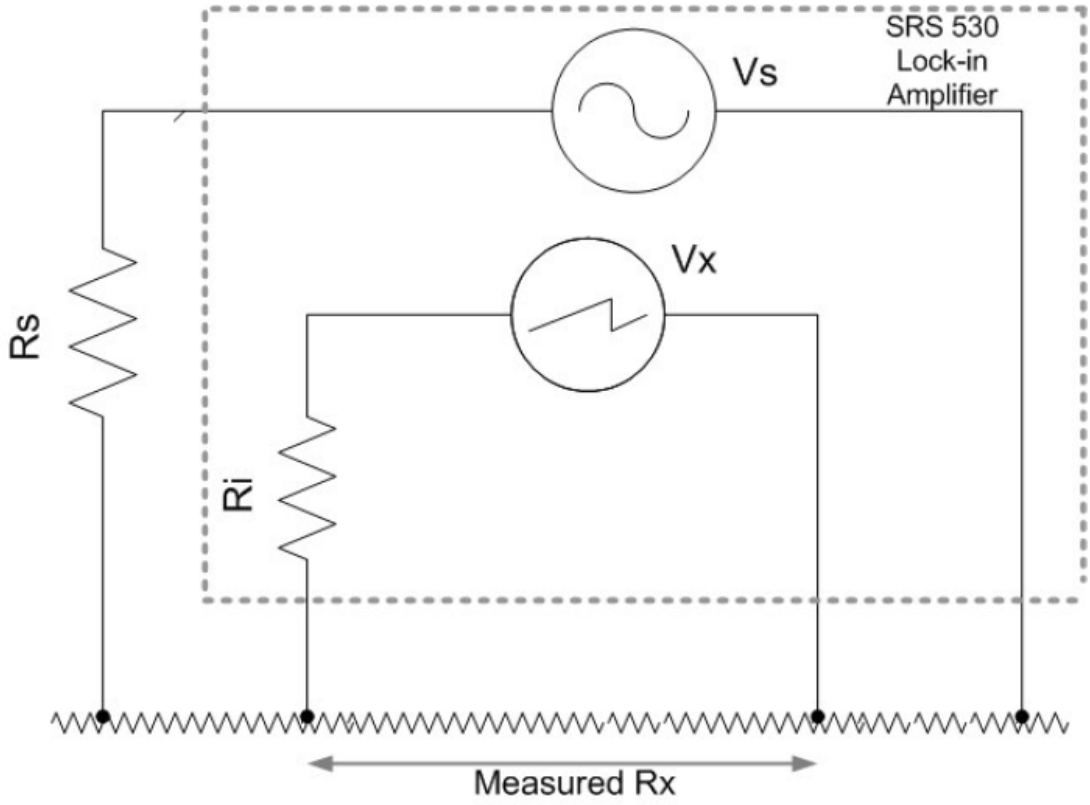

Figure 10. Schematic of the four point probe method.[44]

In this method, a current is passed through the sample using the outer probes, while a voltage drop is measured across the inner probes. The advantage of using the four point method is that contact resistance is accounted for directly. A Stanford Research Systems lock-in amplifier (SRS 530) was used to measure the voltage drop V_x and to provide the reference sinusoidal voltage V_s. A reference frequency of 1 KHz was selected. This frequency is high enough to avoid power line and 1/f noise, and also low enough to avoid phase-shift and amplitude errors caused due to the RC time constant of the source

impedance and the cable capacitance.[44] The parameters of the four point probe set-up are listed in Table 1.

Table 1. Parameter values used for resistivity measurements.

Parameter	**Symbol**	**Value**
Source Voltage	V_s	100 mV
Measured Voltage Drop	V_x	1-10 μV
Series Resistance	R_s	7.958 kΩ
Resistance of Sample	R_x	< 1 Ω
Input Impedance	R_i	100 MΩ

Because $R_i >> R_s >> R_x$, circuit theory allows for the simplification:

$$I = \frac{V_s}{R_x + R_s} = \frac{V_x}{R_x} \quad \textbf{(9)}$$

By definition:

$$R_x = \frac{\rho L}{A} \quad \textbf{(10)}$$

Therefore:

$$\rho = \frac{R_s V_x A}{(V_s - V_x)L} \tag{11}$$

Here L is the length of the line, which was measured using an optical microscope with a reticule set at 100 μm, giving a length measurement resolution of ±50 μm. A is the cross-sectional area of the line, determined by taking the average from several profilometry scans.

For each sample, the resistivities of two segments of each serpentine were measured, with 4 different length measurements from each segment. Therefore, eight resistivity measurements were averaged to obtain each sample resistivity. The probe station was calibrated using a known resistor of similar resistance to the deposits.

3.7 X-RAY DIFFRACTION ANALYSIS PROCEDURE

X-ray diffraction patterns were obtained for all of the serpentine pattern samples. A Scintag X-1 θ-θ diffractometer with a solid-state detector using Cu Kα radiation was used to obtain all of the patterns. Each scan covered 30-90° (2θ), with a step size of 0.04 degrees and a dwell time of 6 seconds. This 2θ range included the (111), (200), (220), (311), and (222) peaks. The (111) peak had an intensity of about 1500 counts for each of the serpentine samples and the average background was about 50 counts.

MDI's Jade 7 software was used to analyze the patterns. For grain size analysis, the background was removed and a profile was fitted to all five peaks. Grain size analysis from x-ray diffraction is based on the Scherrer equation:[56]

$$\beta = \frac{\lambda}{t\cos\theta} \quad \textbf{(10)}$$

where β is the width of the peak at half maximum, λ is the wavelength of the x-ray radiation, θ is the angle of diffraction, and t is the crystal size.

A Williamson-Hall plot[57] is obtained by plotting β cos θ versus sin θ and is used to assess the relative contributions to diffraction peak broadening from strain and grain size. Each diffraction peak is represented by a point on the plot, and all the diffraction peaks from a pattern are represented on the same plot. Fitting a line to the data allows the grain size and magnitude of the strain to be determined. The y-intercept on a Williamson-Hall plot is related to the grain size, while the slope of a line is related to strain inherent to the sample. Jade was used to generate and analyze a Williamson-Hall plot for each sample (after accounting for instrument broadening).

3.8 CALCULATION OF DENSITY

Direct measurement of the density of the Ag deposits was not conducted due to the difficulty of accurately measuring the small mass of deposits such as ours. Instead, the density was inferred by analyzing the resistivity of the deposits with respect to the

grain size (obtained from X-ray analysis), and then fitting the data to a model. Qin's model uses a transmission coefficient (T*) for electrons through a boundary, which relates the effects of grain boundary scattering and density changes on conductivity thusly:

$$\sigma = \frac{1}{\rho} = \frac{1}{\rho_{bulk}} \frac{\lambda_{bulk}}{\lambda'} T^{*\lambda'/d} \quad \textbf{(11)}$$

where σ, ρ, ρ_{bulk}, λ_{bulk}, λ', and d are the conductivity, resistivity, bulk resistivity, bulk mean free path, sample mean free path, and grain size. Qin experimentally determined a linear relationship between ln(T*) and 1/D, where D is the fractional density of the nanostructured Ag. We assumed a linear relationship between mean free path and grain size for grains smaller than 51 nm, which is also consistent with Qin's experimental results. After directly measuring the grain size (using XRD) and resistivity of our deposits, we calculated T*, and therefore were able to compute the density for each sample.

Chapter 4: *Results*

4.1 General Characterization of Deposits

Figure 11 shows TEM images of Ag NPs produced in He by the LAMA process. Previous work on Ag NPs produced by LAMA in He indicated an average particle size of 6 nm.[29] Figure 11(a) shows a high resolution TEM of a single NP, showing the spherical and crystalline nature of a typical NP produced by LAMA. The size of the particles ranged from approximately 2 to 60 nm. Figure 11(b) shows one particle that is much larger than the typical NPs, which can be seen surrounding this large NP. This micrograph illustrates the approximate range in particle sizes produced under the processing conditions used in our study.

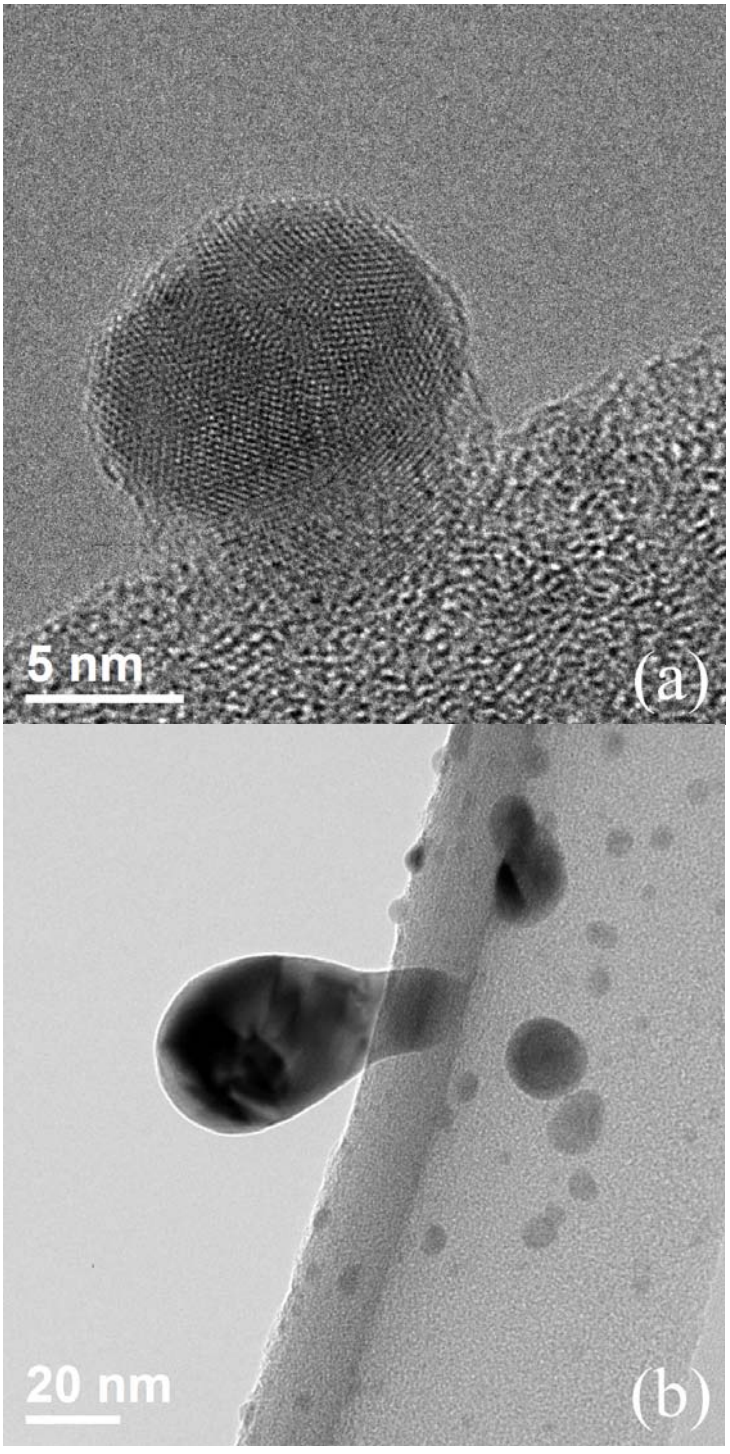

Figure 11. TEM images of Ag NPs produced by the LAMA process.

Figure 12 shows an SEM image of a cross-section of an as-deposited Ag line, showing the pseudo-Gaussian profile typical of our deposits.

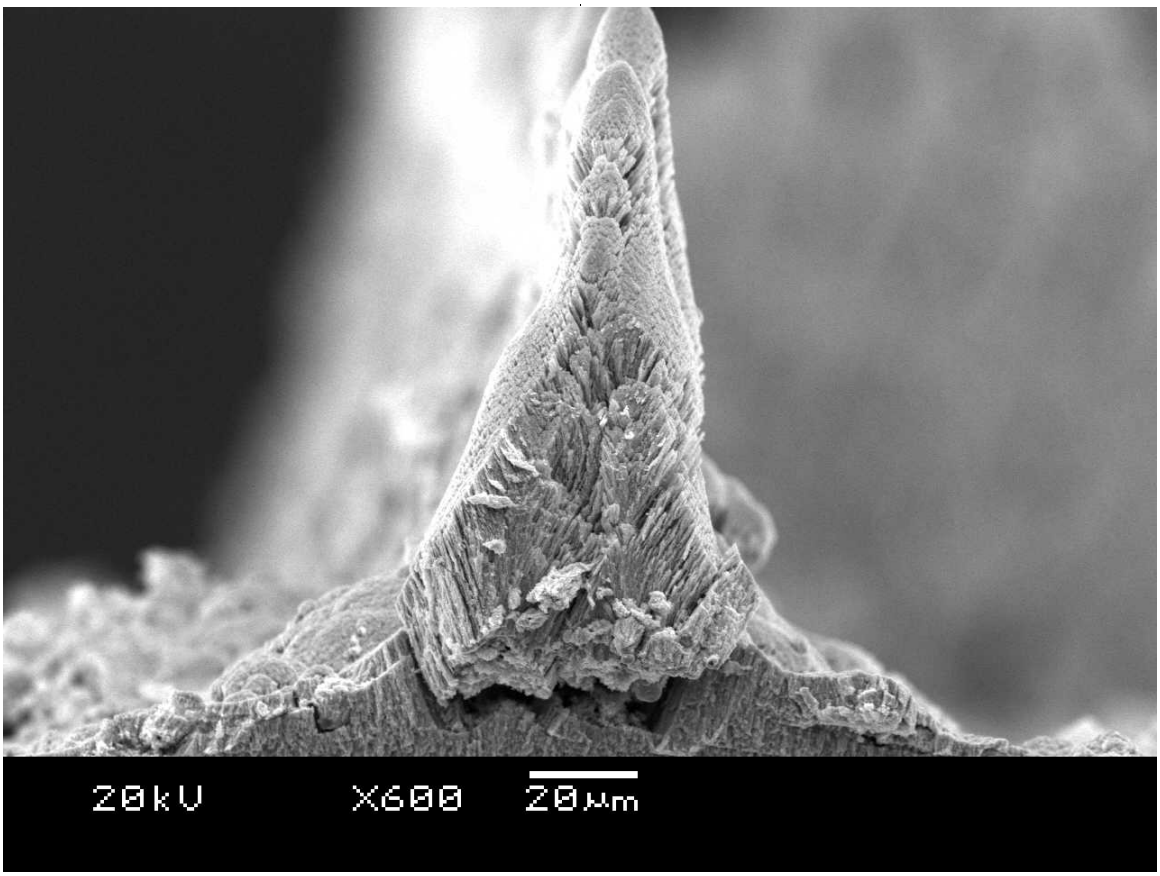

Figure 12. SEM image of a cross-section of an as-deposited line.

There are considerable height variations along the length of as-deposited samples, illustrated in Figure 13(a) and (b). Figure 13(a) shows an SEM image of a plan-view of an as-deposited line, with the line oriented horizontally. Figure 13(b) is an angled view of the same line that highlights the non-uniform height along the length of the line shown along the top of the image.

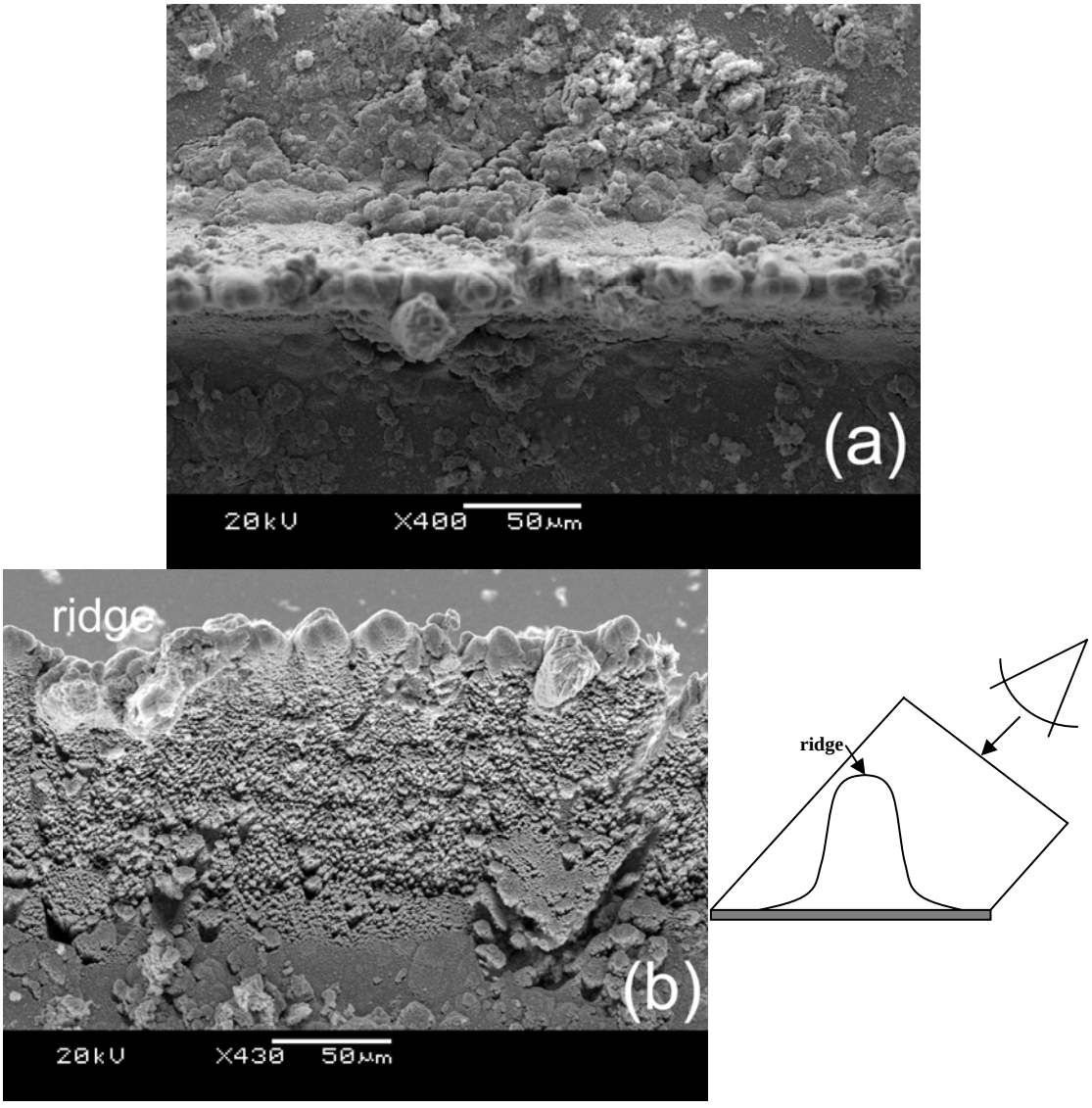

Figure 13. SEM images of a plan view (a), and an angled view (b) of an as-deposited line.

Figure 14 shows an amalgamation of three different line profiles measured using profilometry, showing that the thickness of most of the deposits produced for strength testing ranged from 30 to 110 μm. The thickness of the deposits depended on the processing conditions as well as the number of passes used to produce the samples. These profiles are typical of lines of similar deposition thickness.

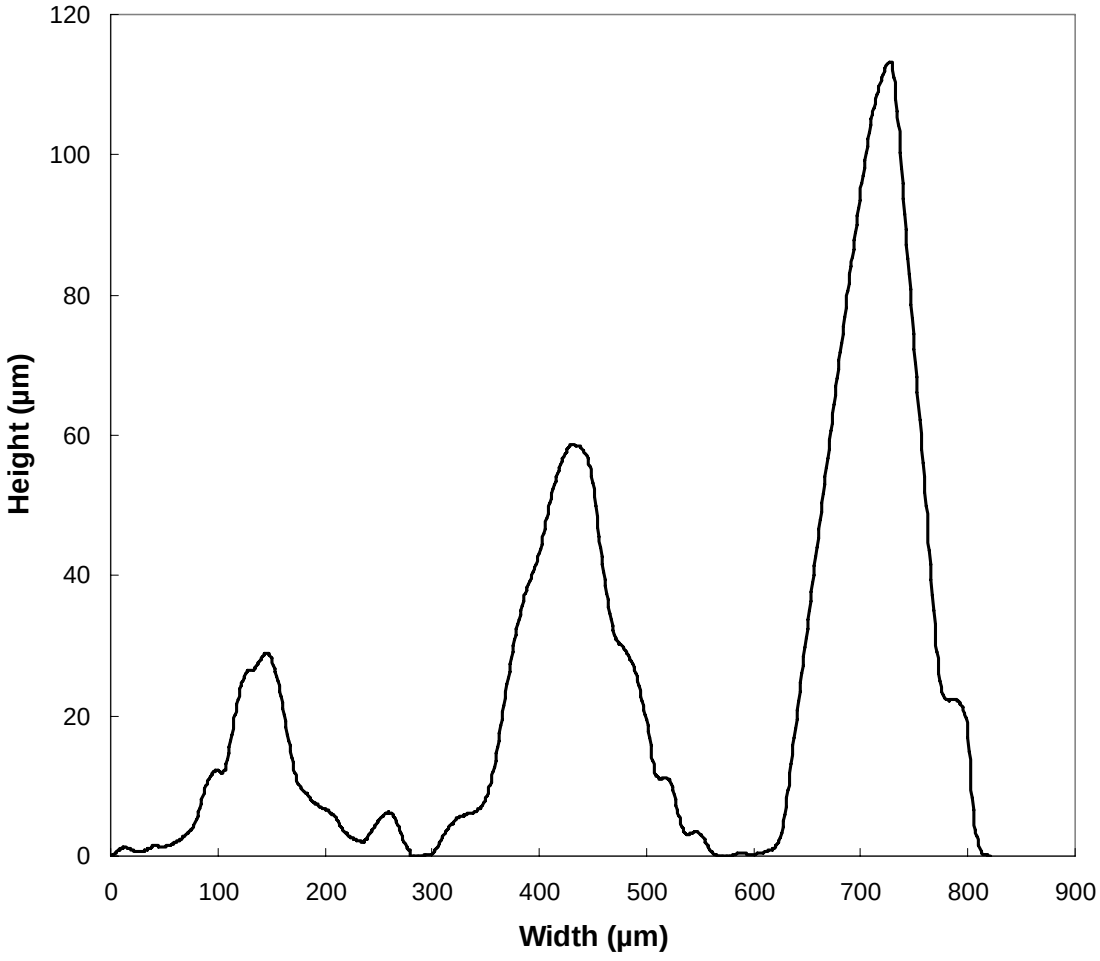

Figure 14. Typical profiles from three samples of different thicknesses.

Note that the base width of the deposited lines does not vary significantly with deposition thickness. Because the base width does not vary significantly with peak height, the full width at half maximum of the lines is not a strong function of peak height. Typical profilometry scans for the serpentine samples are presented in Figures 15 and 16.

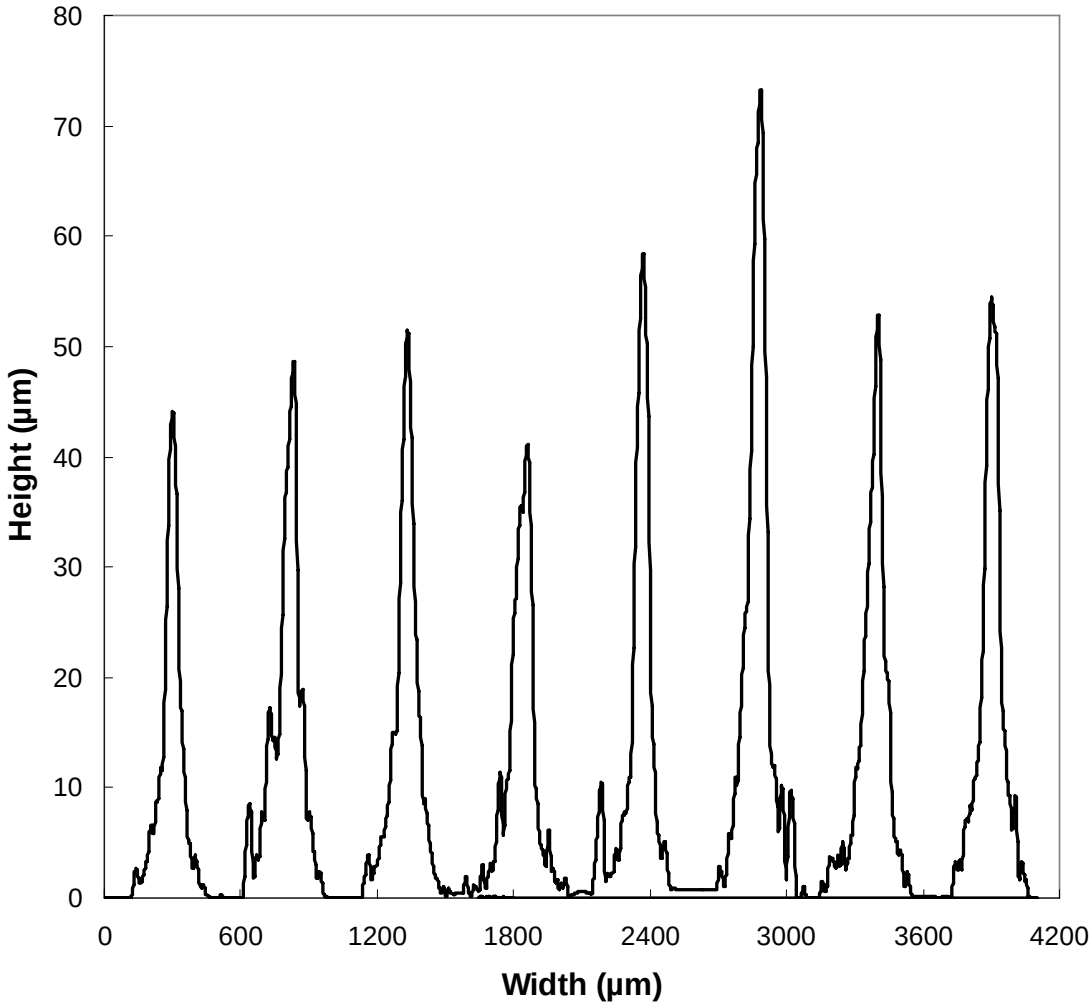

Figure 15. A profilometry scan across all eight lines of a thick as-deposited serpentine sample.

While most of the serpentine samples were between 20 and 80 μm thick (Figure 15), there were four samples that were in the 13 to 20 mm range (Figure 16). These four samples were used for the samples processed without a compression load, while the thicker samples were processed under load.

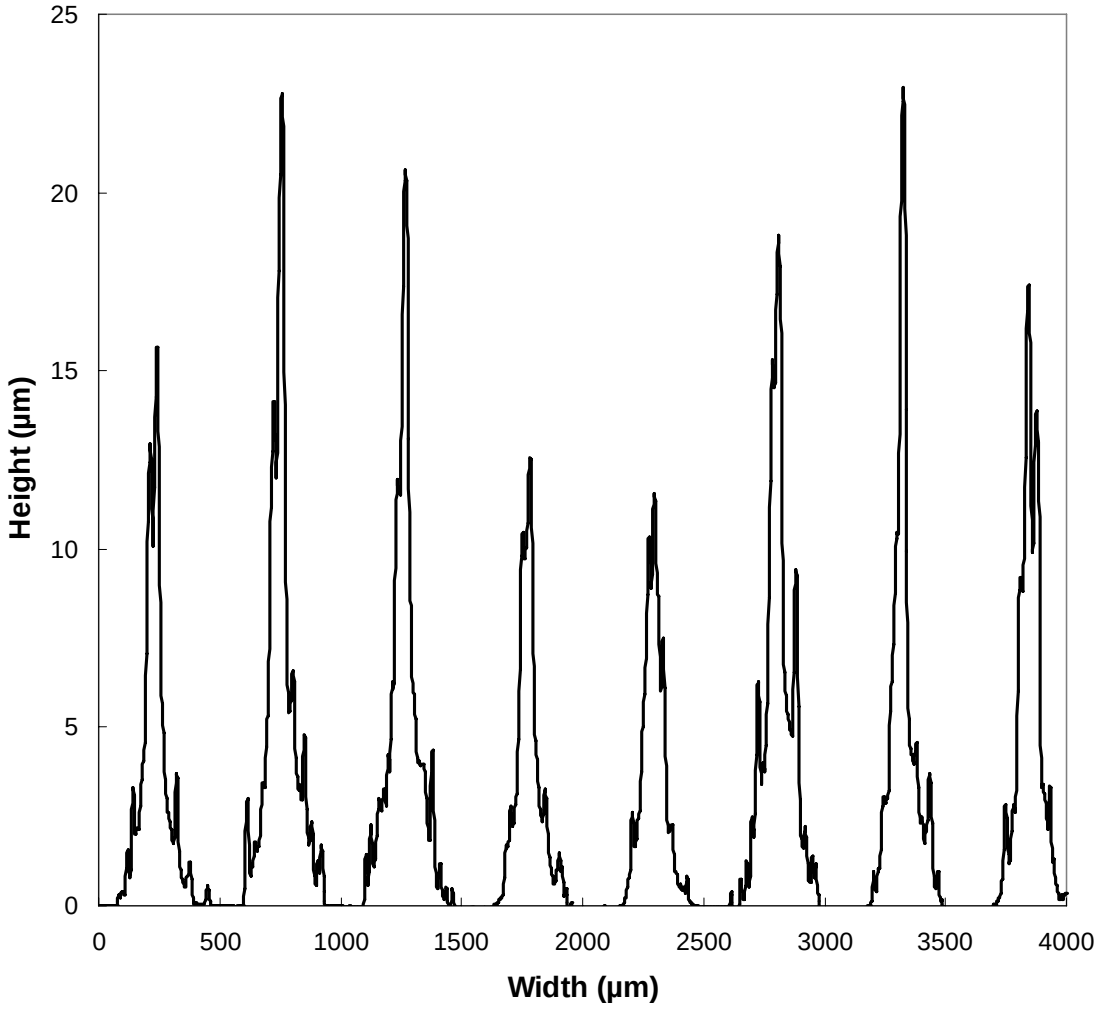

Figure 16. A profilometry scan across all eight lines of a thin as-deposited serpentine sample.

During compression, the top of a line is flattened by the blank substrate. Because of the contact between the flat substrate and the approximately Gaussian deposit, the pressure distribution is non-uniform during compression, as shown schematically in Figure 17.

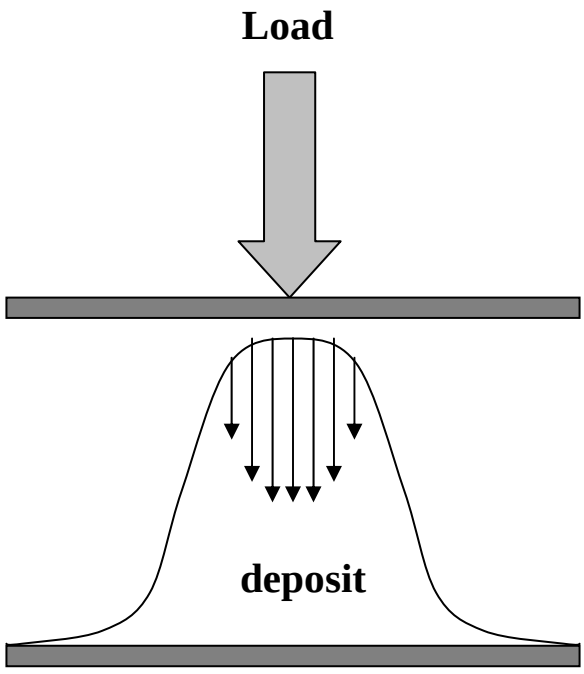

Figure 17. Schematic of a cross-section of a line and the pressure distribution during compression.

SEM analysis of the compressed samples showed evidence of non-uniform densification resulting from the non-uniform pressure distribution during compression.

Figure 18 shows a series of images of increasing magnification showing a region of higher density. Figure 18(a) shows darker contrast along the centerline of a Ag deposit, indicating regions of high density. These regions are shown in more detail in Figures 18(b) and 18(c).

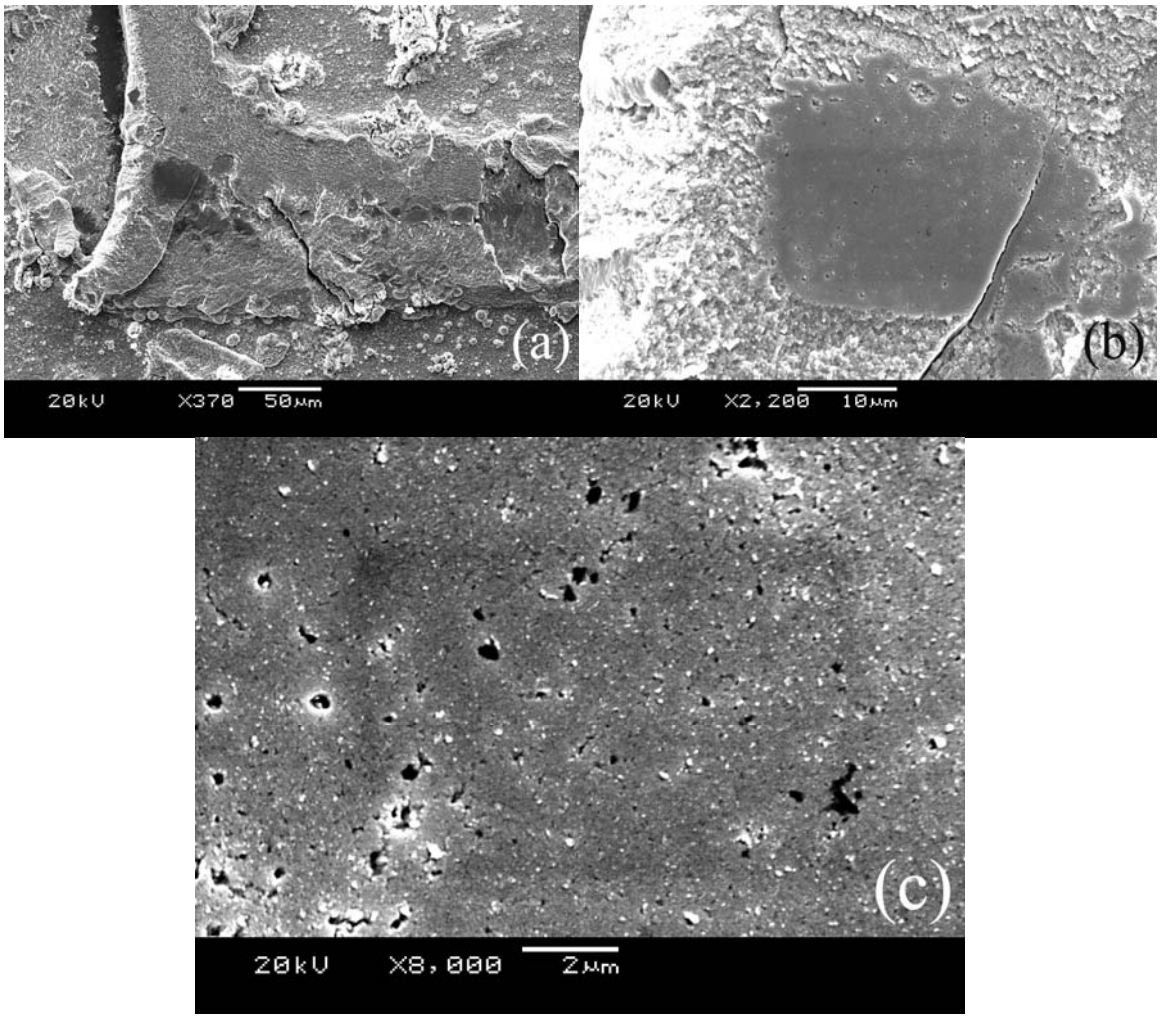

Figure 18. SEM image series of a sample after compression and then tension testing. The darker contrast in (a) and (b) indicates regions of higher density.

4.2 STRENGTH

The strength of the bonded samples was tested as a function of processing temperature and the compressive load applied during bonding, for samples of different line thicknesses. While samples processed under identical conditions showed similar strengths, the scatter in the strength plots implies a significant amount of variability from sample to sample. Therefore, the data presented here illuminates general trends associated with the variation of processing conditions.

The influence of deposit thickness on the bond strength is shown in Figure 19. The strength of the lines varied from nearly zero to greater than 100 MPa. However, it is apparent that there is not a strong correlation between bond strength and the deposit thickness.

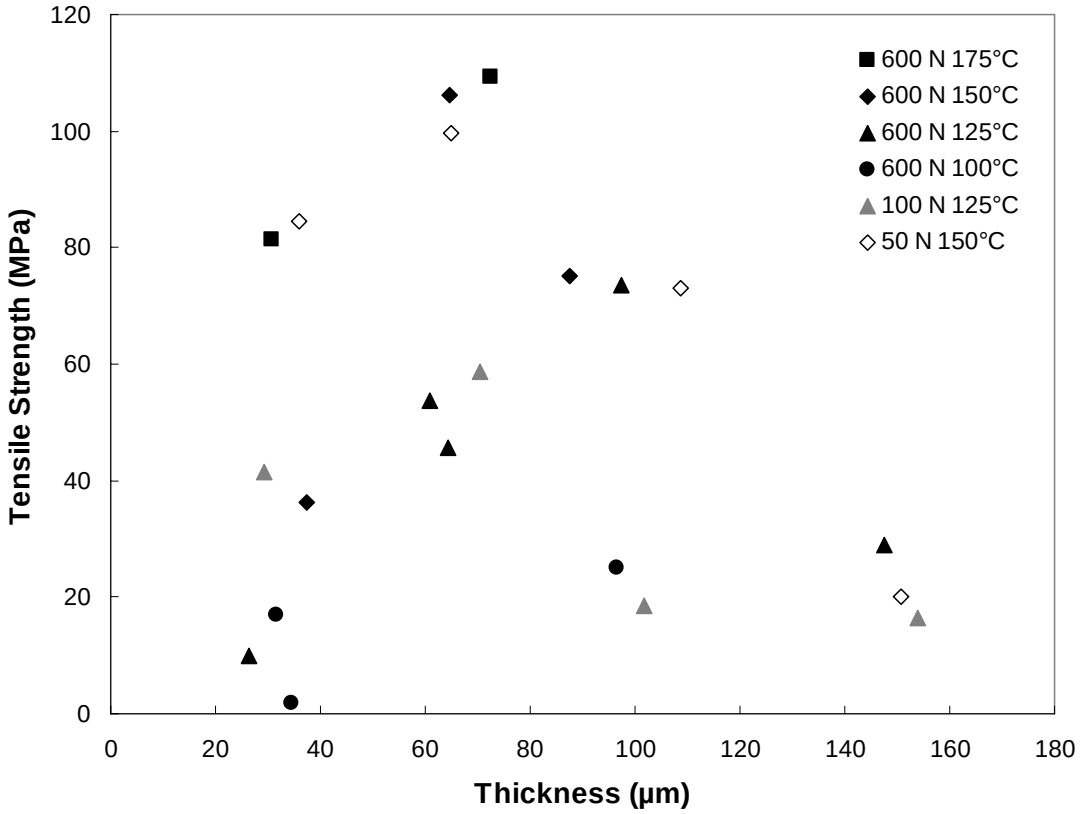

Figure 19. Effect of deposition thickness on tensile strength. The legend indicates the compressive load and temperature applied during bonding.

The influence of compressive stress applied during bonding on the subsequent tensile bond strength is shown in Figure 20. The data show that the bond strength is relatively insensitive to the compression loads that were applied during bonding. This range of loads corresponded to mean stresses typically ranging from 200 - 500 MPa.

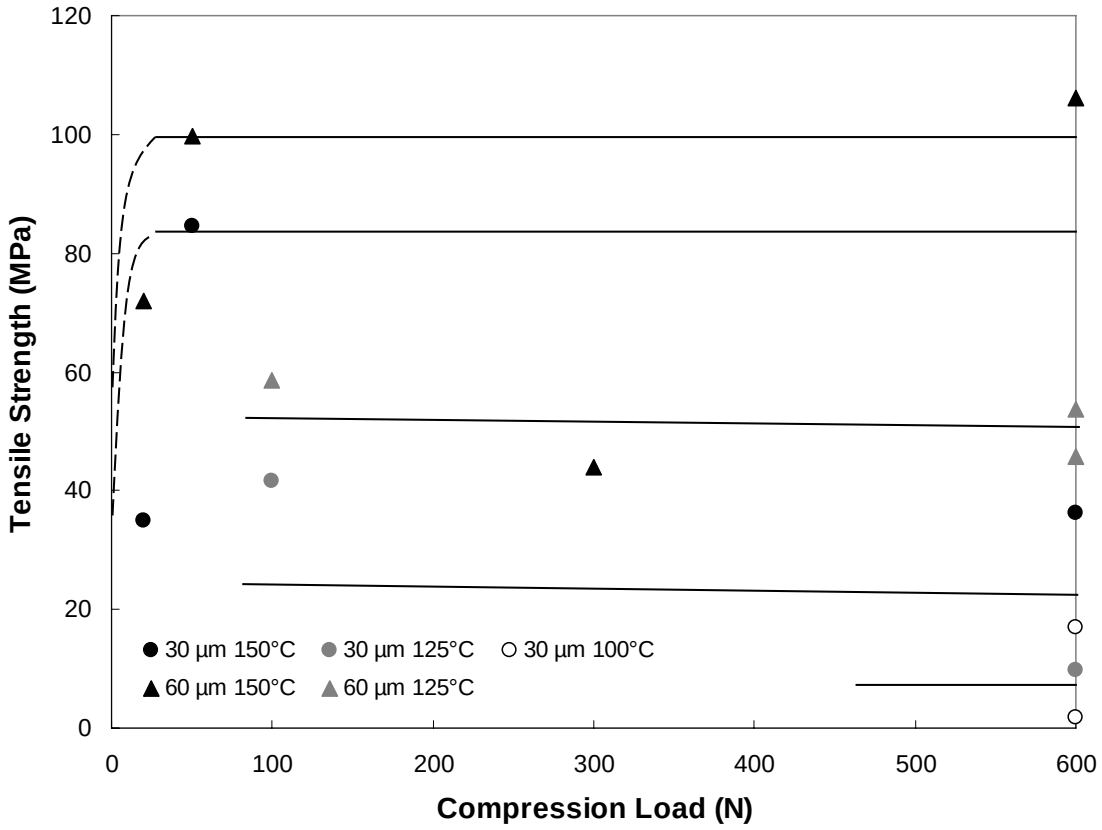

Figure 20. The effect of compression load on tensile strength. Trend lines are solid, while dashed lines indicate the expected trend with no compression load. The legend indicates the approximate thickness of the deposit and the temperature of the sample during bonding.

Compression load was varied over more than an order a magnitude (50 - 600 N) with no identifiable trend in the resulting strength data. There was a significant amount of apparent scatter in the data (up to a factor of 2 for tensile strength), but this is relatively small compared to the range of compressive loads tested.

It is possible that this range of compressive stresses is above a threshold value, beyond which stress has no strong effect on the resulting sample strength. For samples compressed at very low loads (20 N) the bond strength appears to be reduced compared to samples compressed at higher loads, but due to the scatter in the data, this is not statistically significant. These results are in general agreement with the results of Schwarzbauer and Kuhnert who show a similar plateau behavior in bond strength at high compressive stresses.[16]

The tensile strength of bonded specimens is shown as a function of processing temperature in Figure 21. It is clear from this figure that, despite considerable scatter in the data, there is a strong correlation between bond strength and the temperature at which the samples were bonded. Increasing the processing temperature consistently increased the strength of the samples. The dashed line represents the overall trend, while the solid lines are trend lines for individual data series. Increasing the processing temperature from 100°C to 175°C increased sample strengths from approximately 20 MPa to over 100 MPa.

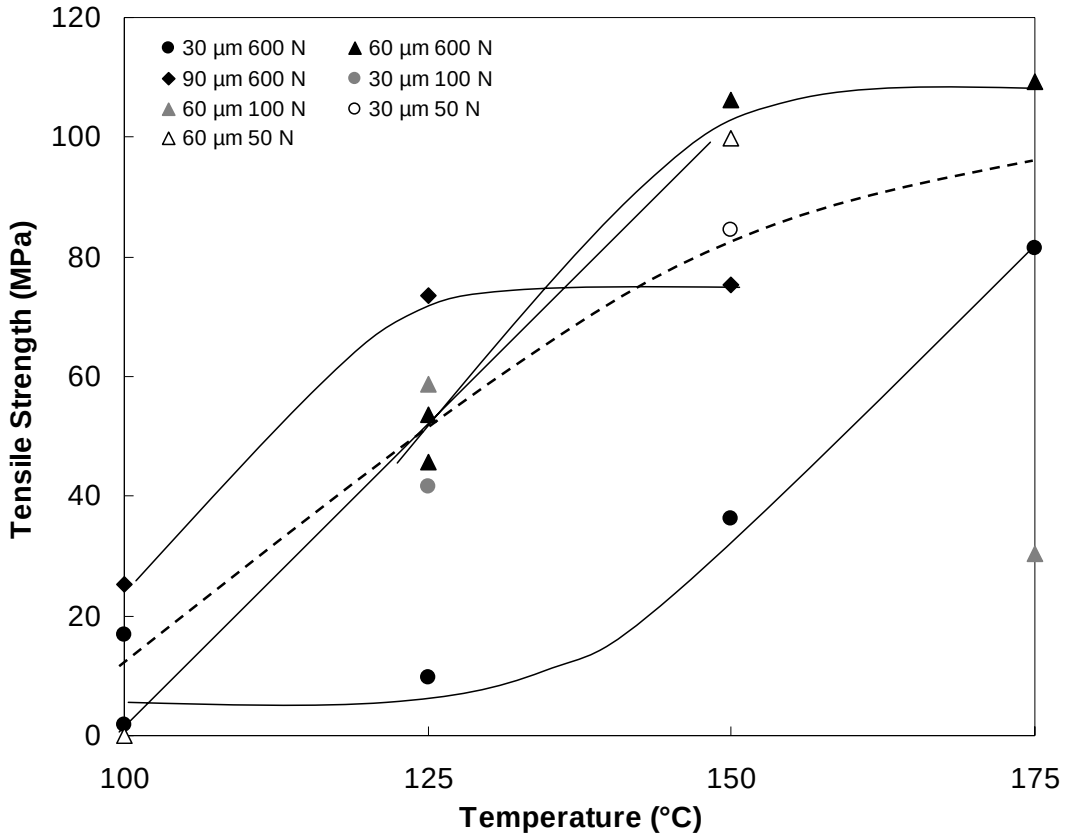

Figure 21. The effect of temperature on tensile strength. The legend indicates the approximate thickness of the deposit and the compressive load applied during bonding.

All samples tested exhibited mixed mode failure, where the fracture propagated through the Ag deposit, the Au/Cr layer, and the Si wafer, as shown in Figure 22(a) and (b). Figure 22(a) shows a region where the Ag deposit was debonded from the deposition substrate during tension testing. Figure 22(b) shows a region where fracture propagated through the Si from the top substrate, leaving Si bonded to the deposition substrate after fracture.

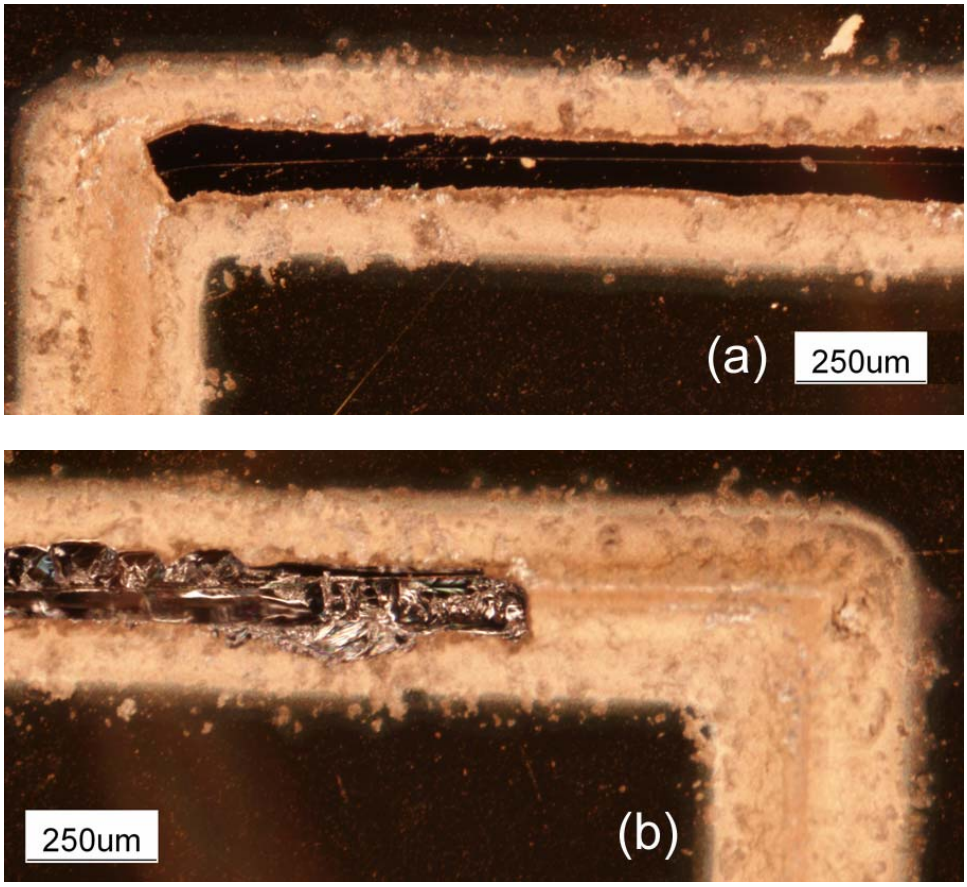

Figure 22. Regions of a sample where Ag debonded from the deposition substrate during fracture (a) and where fracture propagated through the Si of the top substrate, leaving Si bonded to the deposition substrate (b).

Observations of even the lowest strength samples showed the presence of Ag on both the bottom and top substrates, as shown in Figure 23.

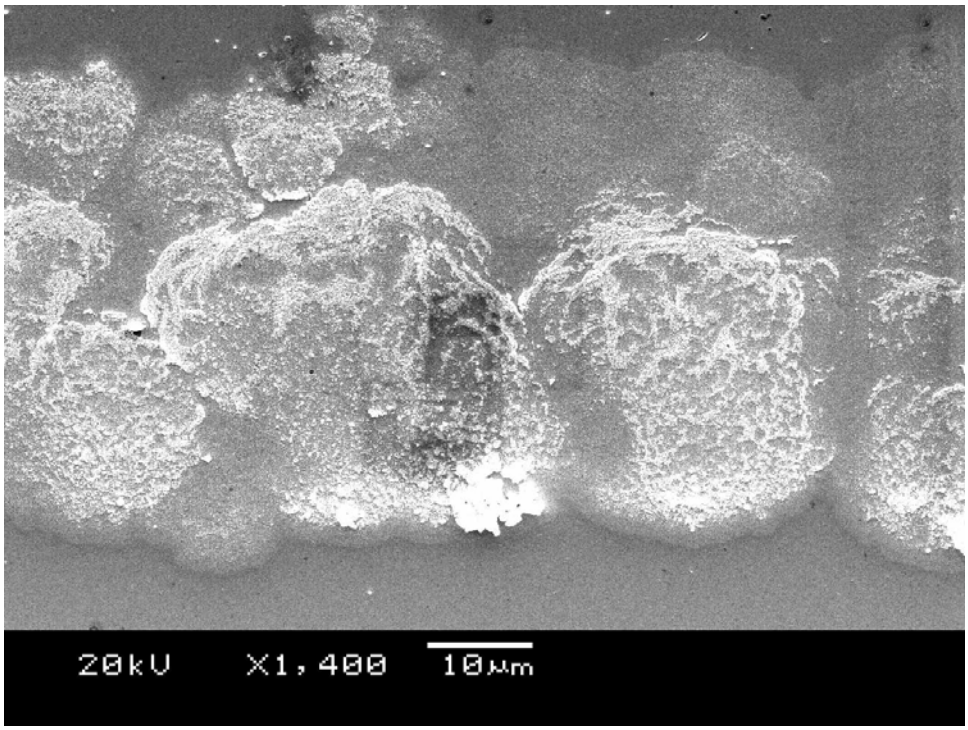

Figure 23. Plan-view SEM showing material transferred to the top blank substrate during bonding on a low strength sample.

Figure 24 shows an EDS spectrum confirming the presence of Ag, along with Cr, Au, and Si from the substrate, on the top blank substrate for a low strength sample.

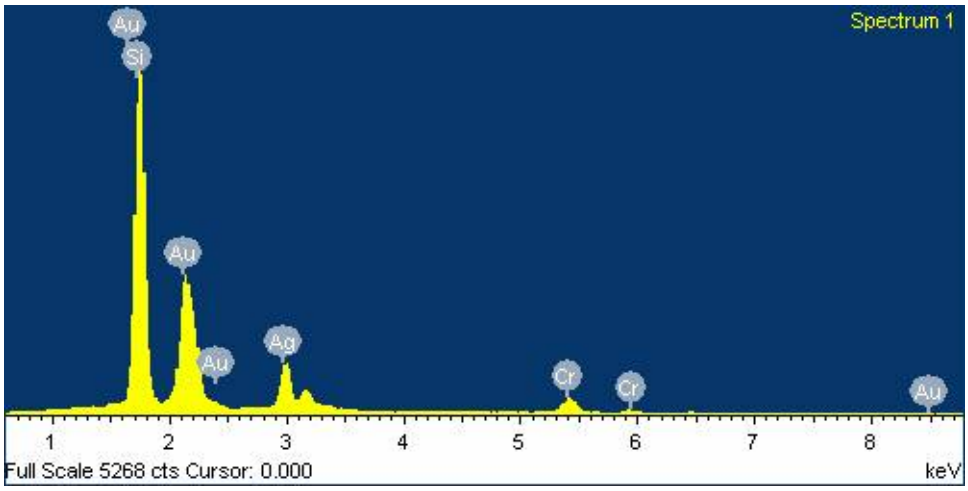

Figure 24. EDS spectrum from a low strength sample blank substrate.

This indicates that, even for samples that were not well-bonded, at least parts of the sample failed within the silver deposit rather than at the interface between the silver and the metal bondcoat. Therefore, even for these low strength samples, some degree of bonding occurred between the silver and both substrates. However, it is not possible to determine from the fracture surfaces the origin of the fracture. It is possible that failure may have initiated at the interface of the silver and the metal bondcoat and subsequently propagated through the silver, even for samples with Ag on both the top and bottom substrates.

4.3 RESISTIVITY

For the resistivity measurements, serpentine samples were compressed under varying loads and at different processing temperatures. Although the same loads were used on both the square and serpentine samples, the data cannot be directly correlated across the different types of samples, due to the significantly higher contact area associated with the serpentine samples. A serpentine sample compressed at the same load as a square sample would see roughly one-fourth the compressive pressure.

The resistivity, normalized to the resistivity of bulk polycrystalline silver with conventional grain sizes (>10 μm), is shown in Figure 25.

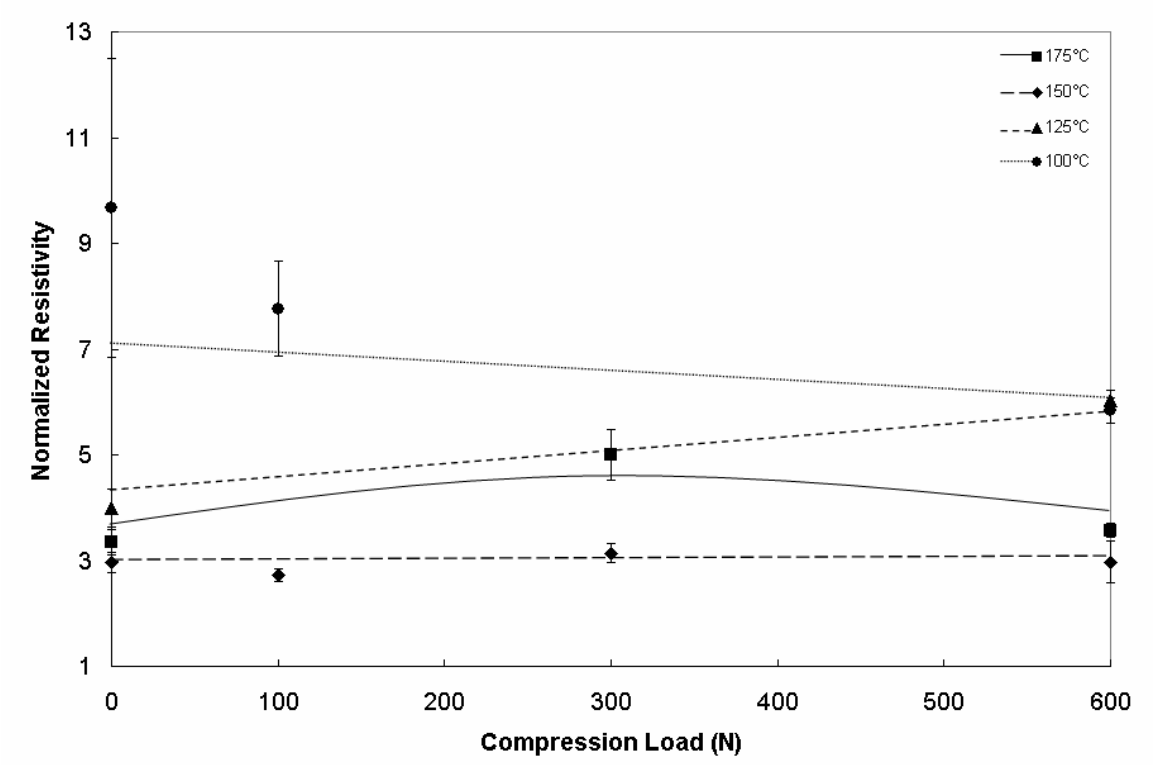

Figure 25. The effect of compression load on ratio of resistivity to bulk. The legend indicates processing temperature.

The error bars in the resistivity ratio plots represent the standard deviation of the resistivity measurements from the same sample. Because there was little effect of compressive load on the strength at high applied compressive pressure, it was expected that processing the serpentine samples at lower compressive pressures might reveal more of an effect of pressure on densification of the samples. However, even at the lower compressive pressures, there was no significant effect of compressive load on the resistivity of the samples.

The influence of processing temperature on resistivity is shown in Figure 26.

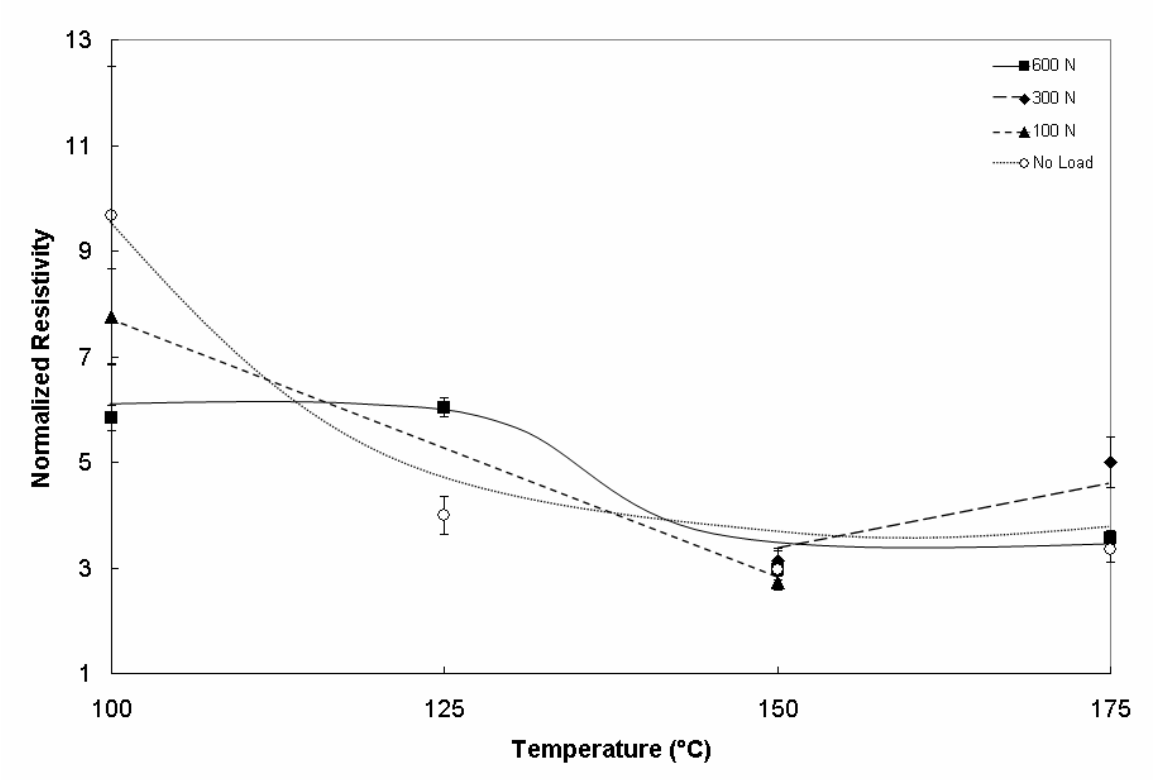

Figure 26. The effect of temperature on the ratio of resistivity to bulk. The legend indicates the compressive load applied.

From this figure it is apparent that increasing the processing temperature decreased the resistivity of the samples. Samples processed at 100°C had resistivities as high as 9.7 times the bulk resistivity of Ag, while samples processed at 150°C had resistivities as low as 2.7 times the bulk resistivity of silver (1.63 μΩ cm).[21] This compares to the previous result of a resistivity of nearly 13 times bulk resistivity for as-deposited Ag produced by LAMA.[44]

4.4 GRAIN SIZE

Grain size of the serpentine samples was determined through X-ray diffraction analysis. Figures 27, 28, 29 and 30 show the X-ray diffraction patterns for samples processed at 100, 125, 150 and 175°C. Note that the (111) peak is approximately 5 times the intensity of the next most intense peaks, and that the differing compression loads do not have an affect on the breadth of the peaks.

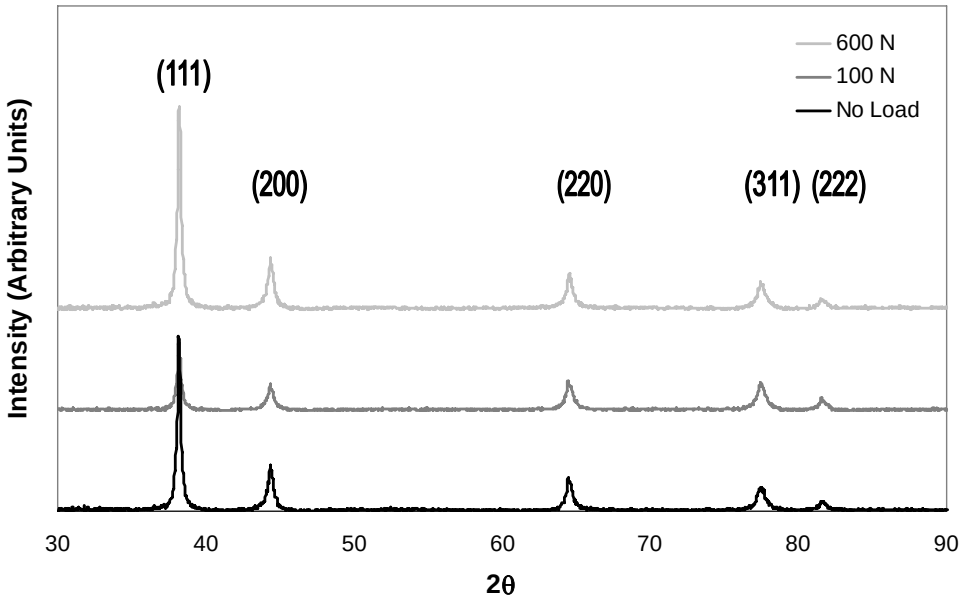

Figure 27. XRD patterns for samples processed at 100°C. The legend indicates the compressive load applied, and the (*hkl*) associated with each peak is indicated above the peak.

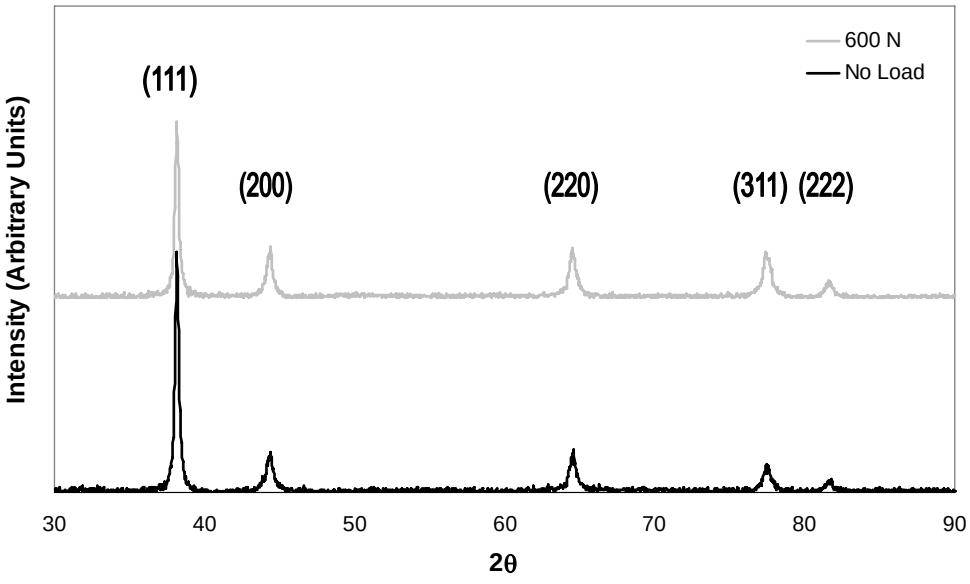

Figure 28. XRD patterns for samples processed at 125°C. The legend indicates the compressive load applied, and the (*hkl*) associated with each peak is indicated above the peak.

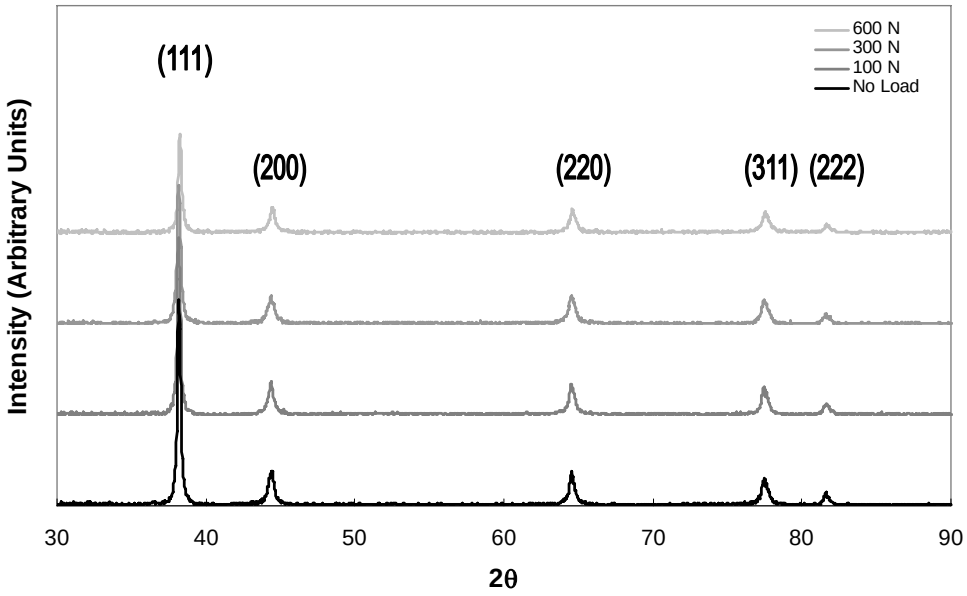

Figure 29. XRD patterns for samples processed at 150°C. The legend indicates the compressive load applied, and the (hkl) associated with each peak is indicated above the peak.

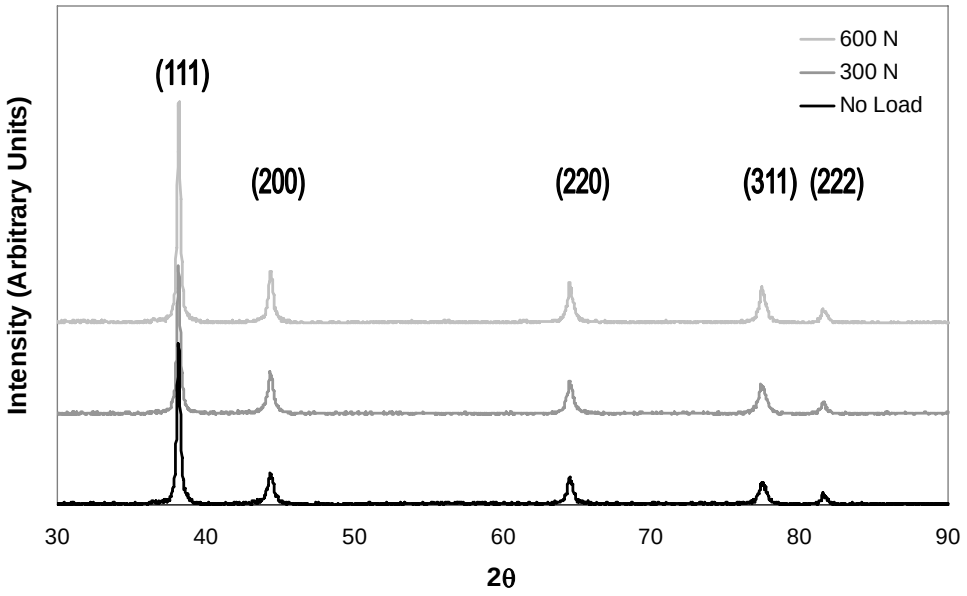

Figure 30. XRD patterns for samples processed at 175°C. The legend indicates the compressive load applied, and the (*hkl*) associated with each peak is indicated above the peak.

These XRD patterns were used to construct Williamson-Hall plots to determine grain size (Figures 31-34).

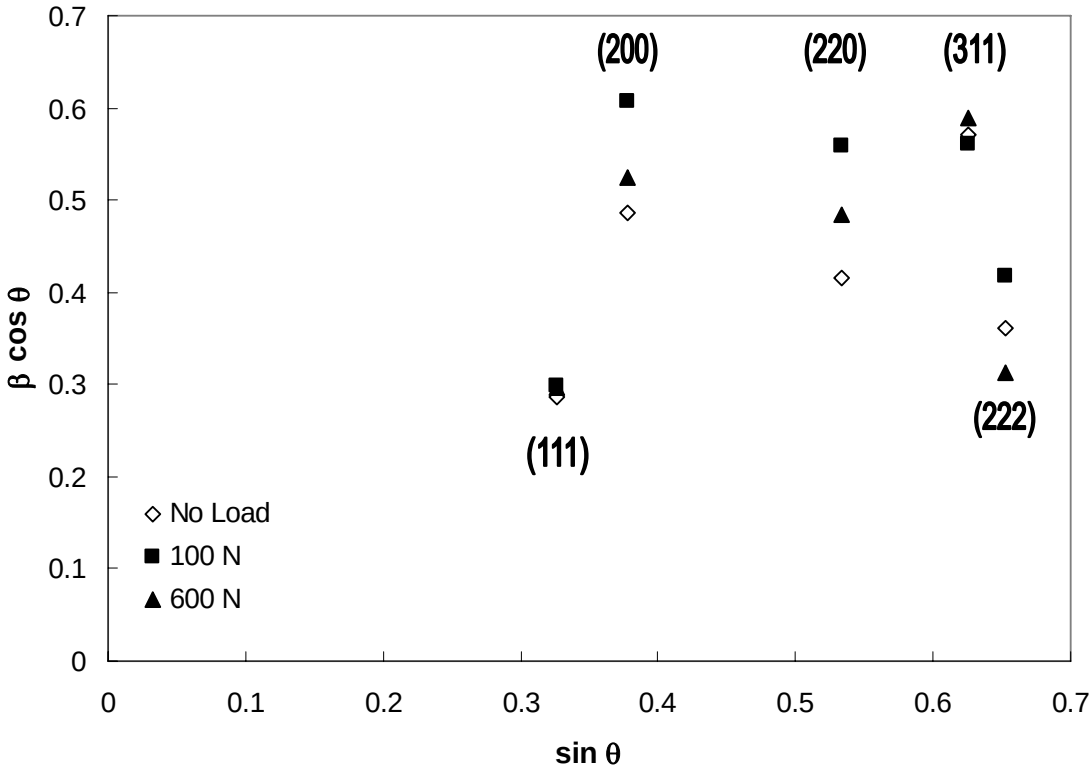

Figure 31. Williamson-Hall plot for samples processed at 100°C. The legend indicates the compressive load applied, and the (*hkl*) associated with each data cluster is indicated next to the data cluster.

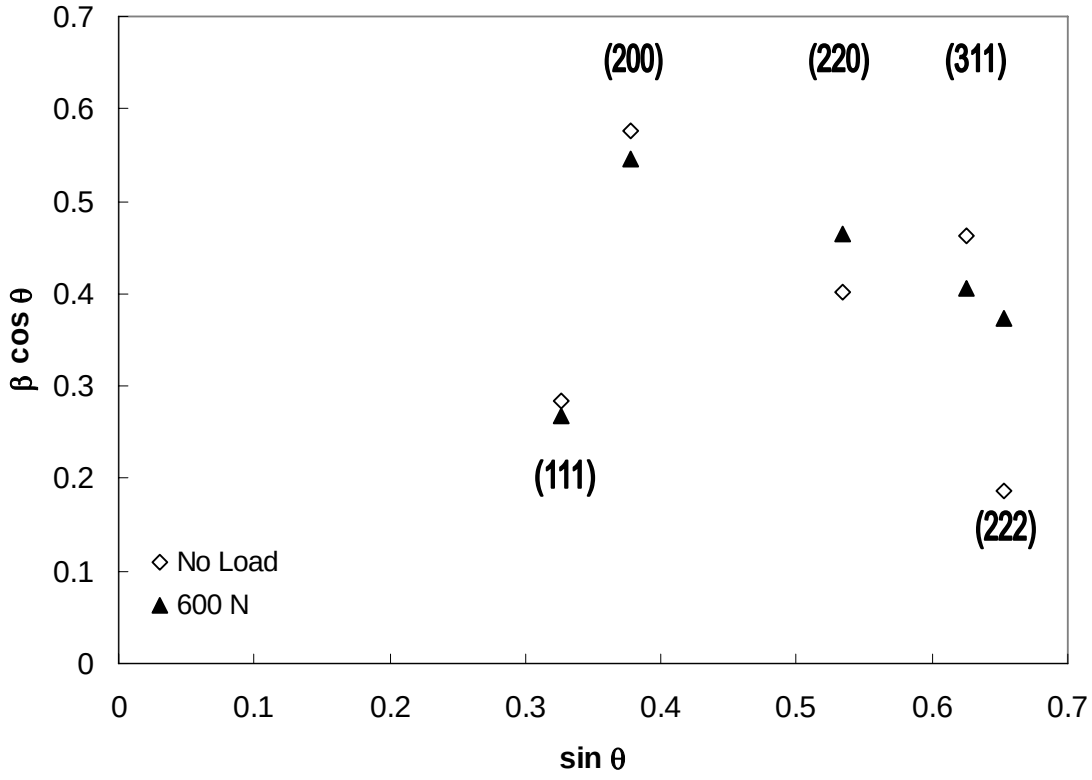

Figure 32. Williamson-Hall plot for samples processed at 125°C. The legend indicates the compressive load applied, and the (*hkl*) associated with each data cluster is indicated next to the data cluster.

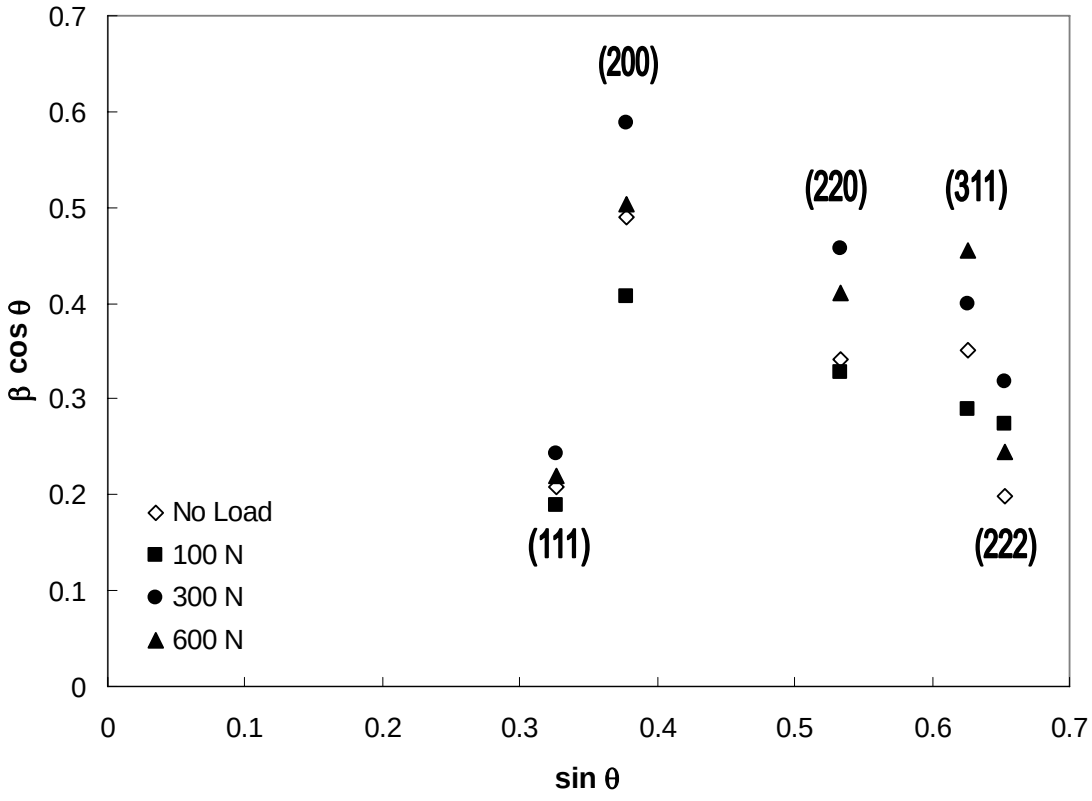

Figure 33. Williamson-Hall plot for samples processed at 150°C. The legend indicates the compressive load applied, and the (*hkl*) associated with each data cluster is indicated next to the data cluster.

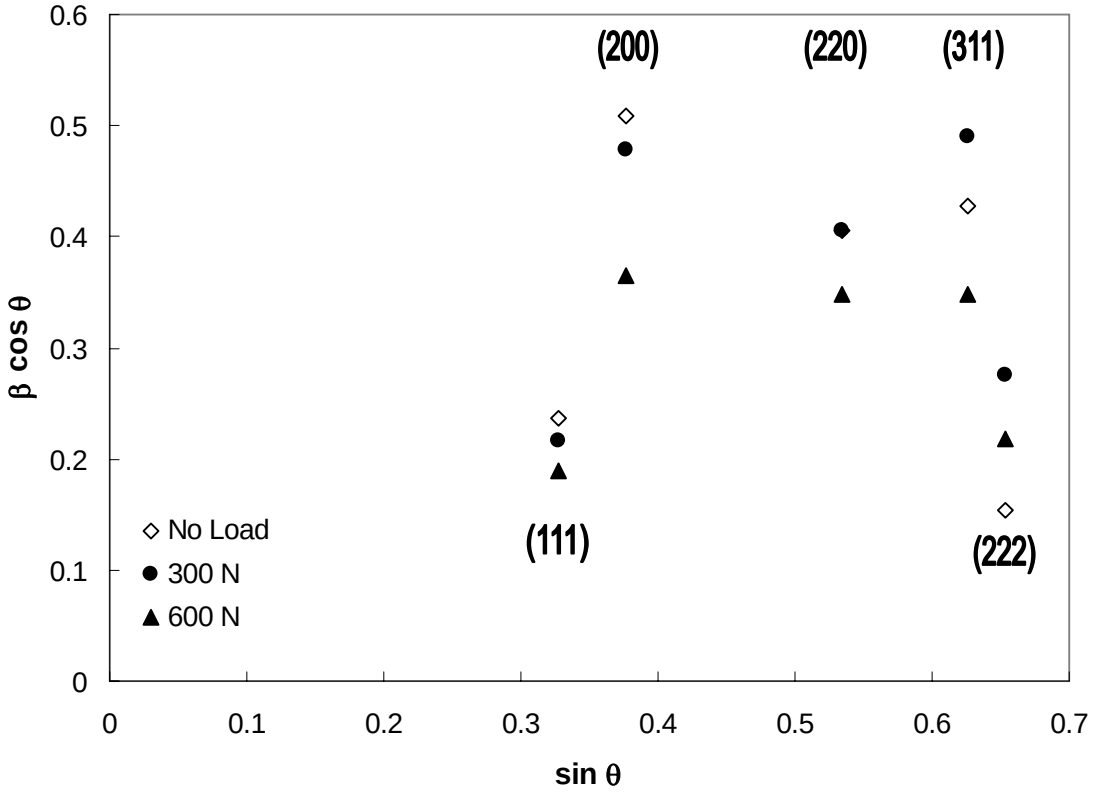

Figure 34. Williamson-Hall plot for samples processed at 175°C. The legend indicates the compressive load applied, and the (*hkl*) associated with each data cluster is indicated next to the data cluster.

From Figures, 31-34, it is apparent that our samples do not show strong evidence of strain (i.e., a straight line with positive slope). In fact, fitting a line through the Williamson-Hall data for some samples produced a non-physical result for grain size since grain size calculated in this manner was negative. Because these results could not be rationalized, we have assumed that the observed peak-broadening was associated with grain size effects rather than strain. Accordingly, only the (111) peaks were used for

grain size analysis because they had about 5 times the intensity of the next most intense peaks, giving a better signal to noise ratio than other peaks.

Figure 35 shows the influence of compressive load applied during bonding on the grain size, as determined from the previous X-ray analysis. From Figure 35, it is clear that grain size does not vary significantly with compression load for any of the temperatures that were studied.

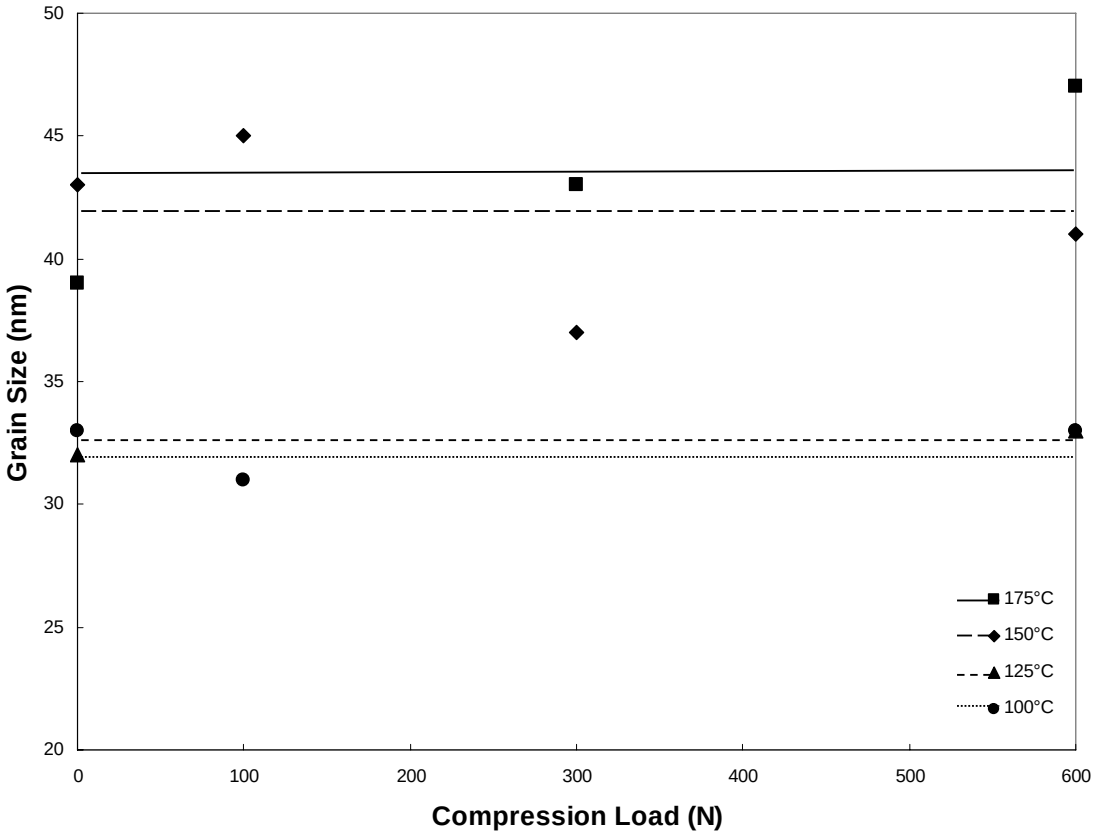

Figure 35. The effect of compression load on grain size. The legend indicates the processing temperature. The horizontal lines indicate the average grain size for all samples processed at the same temperature.

The grain sizes inferred from XRD are shown in Figure 36 as a function of temperature for different compression loads applied during bonding. XRD Scherrer analysis from as-deposited serpentine samples showed an average grain size of 25 nm. Upon heating to 100˚C the grain size increased to just over 30 nm. Figure 36 shows that further increases in temperature resulted in more grain coarsening. Heating to 175˚C resulted in a grain size of 40-45 nm.

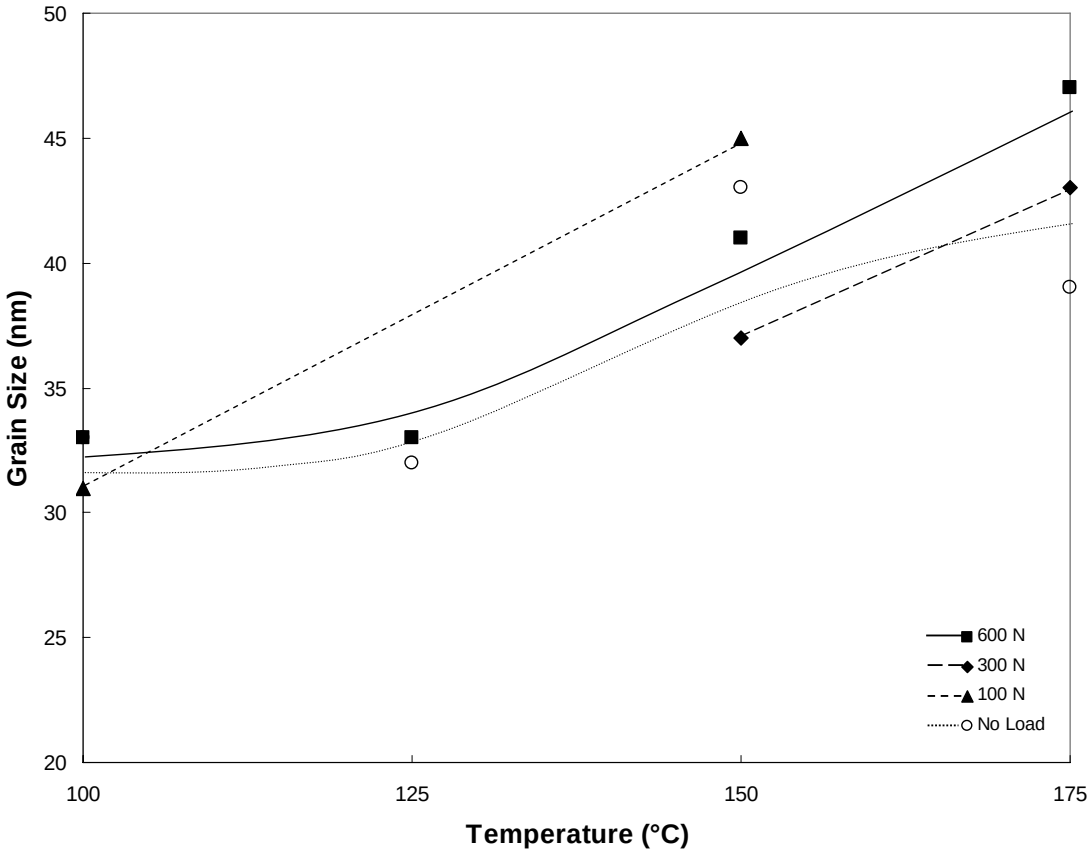

Figure 36. Effect of processing temperature on grain size. The legend indicates the compression load applied. The solid lines tie together samples processed under the same compression load, while the dotted line represents an average grain size for the two samples heated under no load.

4.5 DENSITY

The influence of compression load on the calculated density of the deposits is shown in Figure 37. The average densities range from 75% to as high as 85%.

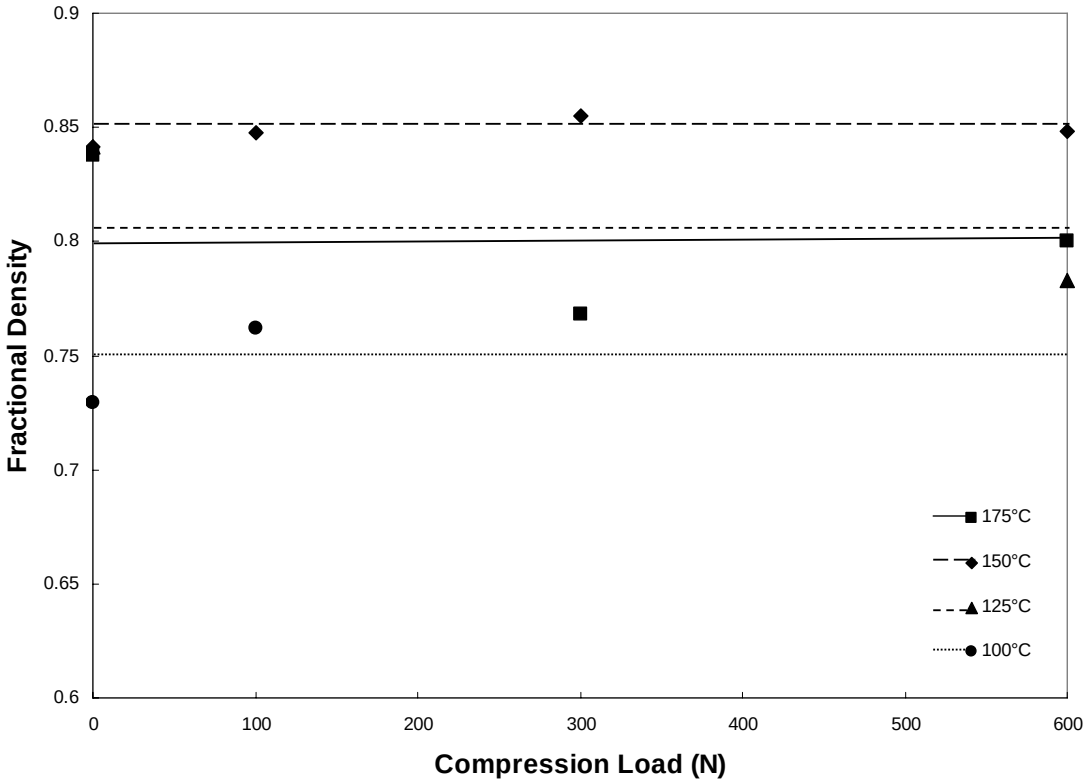

Figure 37. Effect of compression load on density. The legend indicates the processing temperature for the lines.

The horizontal lines represent the average density of all the samples processed at the sample temperature. While this data show higher densities at 150°C than 175°C, this is believed to be due to scatter in the data rather than a result of the process. There does not

appear to be a strong correlation between density and compression load. Note that these densities represent an average density though the line. Given that we have observed non-uniformities in the deformation patterns because of the initially pseudo-Gaussian profile of the lines, it is likely that the actual densities vary significantly with location through the line with the highest densities occurring directly beneath the flat-topped regions of the lines and the lowest densities occurring in the low thickness regions furthest from the peaks of the lines.

The influence of processing temperature on average density is shown in Figure 38. Figure 38 shows that there is a general correlation between processing temperature and density, with increasing density at higher processing temperatures. Samples processed at 100°C had an average density of around 74%, while samples processed at 150-175°C reached an average density of slightly greater than 83%.

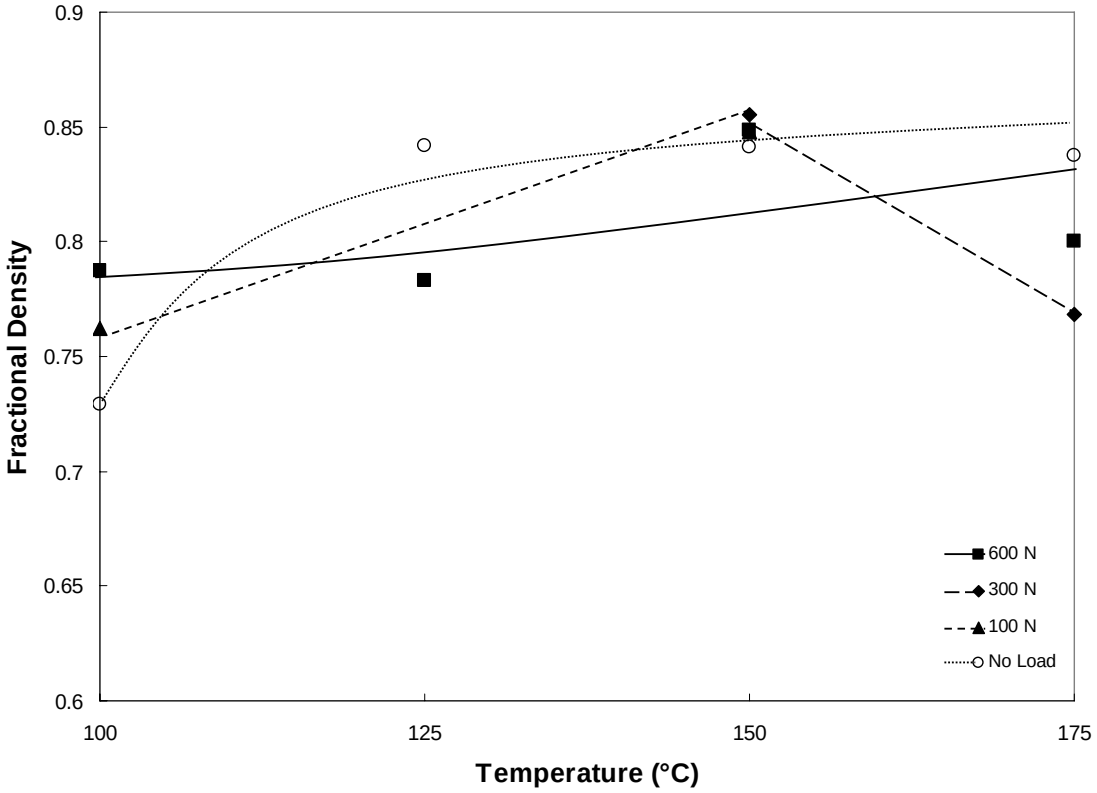

Figure 38. Effect of processing temperature on average density of the deposited lines. The legend indicates compressive load applied. The lines tie together samples processed under the same compression load.

Chapter 5: *Discussion*

In this chapter, the properties of the deposited lines, including strength and conductivity, are compared to previous results. Microstructural factors that influence strength are described and our results are analyzed with respect to these factors and models relating these factors to sample strength. The resistivities of our samples are compared to previous results. Microstructural factors influencing conductivity are also discussed and used to analyze both our work and previous results. Finally, mechanisms responsible for densification and coarsening are assessed and our densification results are compared with theoretical predictions.

5.1 STRENGTH

Figure 39 shows average strength values for our samples compared to previous work in the area. For this plot, our average strengths for each processing temperature were calculated, ignoring the effects of different compression loads. These strength averages were calculated after eliminating the extremely low strength samples associated with each processing temperature, in an effort to present the maximum average strength of a sample processed under our conditions (the full data set was presented in Figure 20). Using this average, our samples exhibited tensile strengths of 21, 55, 91, and 95 MPa for samples processed at 100, 125, 150 and 175°C.

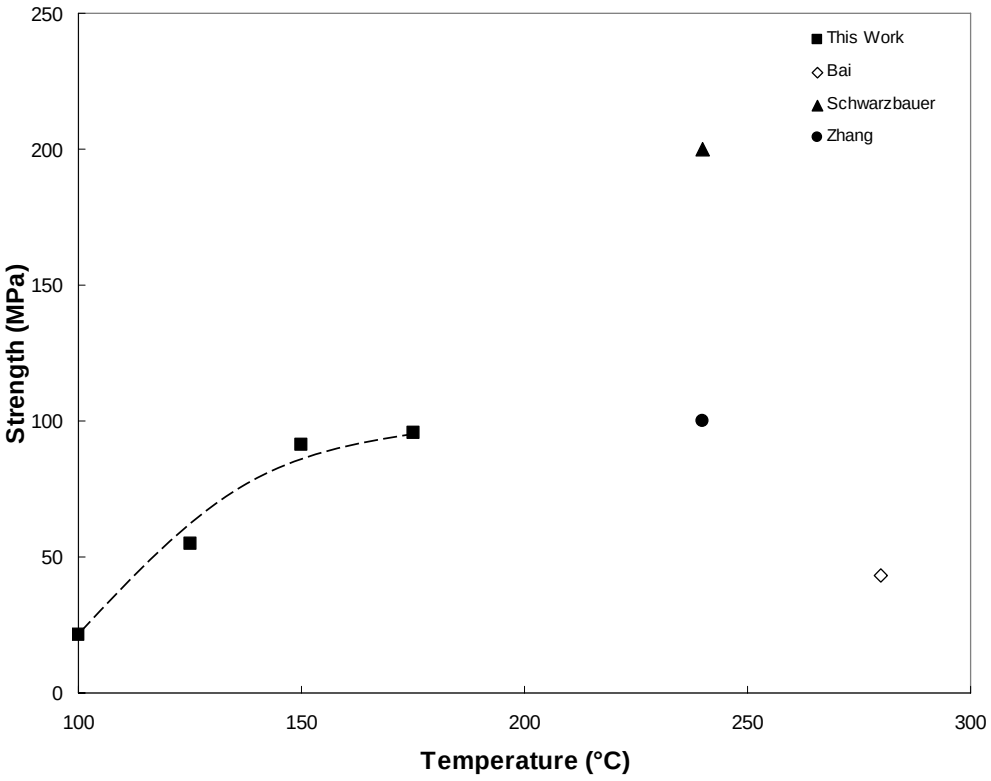

Figure 39. Comparison of strength and processing temperature for related work.[16,18,20]

All of the samples shown used pressure-assisted sintering except Bai et al.'s sample.[20] This seems to indicate that the use of pressure during sintering improves the resulting sample strength. Our samples showed similar strengths to those reported by Zhang et al.[18] While Schwarzbauer and Kuhnert reported higher strengths,[16] it is likely that their higher strengths can be explained by geometric strengthening. Geometric strengthening involves a stronger parent material constraining the deformation of a weaker material at a thin joint. This constraint results in a triaxial stress state on the deposit. Depending on joint geometry and the relative strengths of the deposits and substrates, geometric strengthening can increase the strength of a sample to approximately 3 times the intrinsic strength of the joint material. While our samples had thin joints, the width of the lines was comparable to the thickness of the deposit, not near the factor of 3 required to begin observing geometric strengthening effects.[58] Therefore, our samples exhibited no strength increases due to geometric strengthening effects.

The strength of our samples can be predicted, given the grain size and density, as discussed in Chapter 2. XRD results show that the higher temperature serpentine samples (150 and 175°C) had a grain size of approximately 42 nm, while the lower temperature samples (100 and 125°C) had a grain size of approximately 32 nm. The higher temperature serpentine samples were approximately 83% dense, while the lower temperature samples were approximately 73% dense.

Given Eqs. (2), (3) and (4), as well as Qin's fit to Eq. (2)[41], the predicted strength of nanostructured Ag based on grain size and density can be plotted (Figure 40).

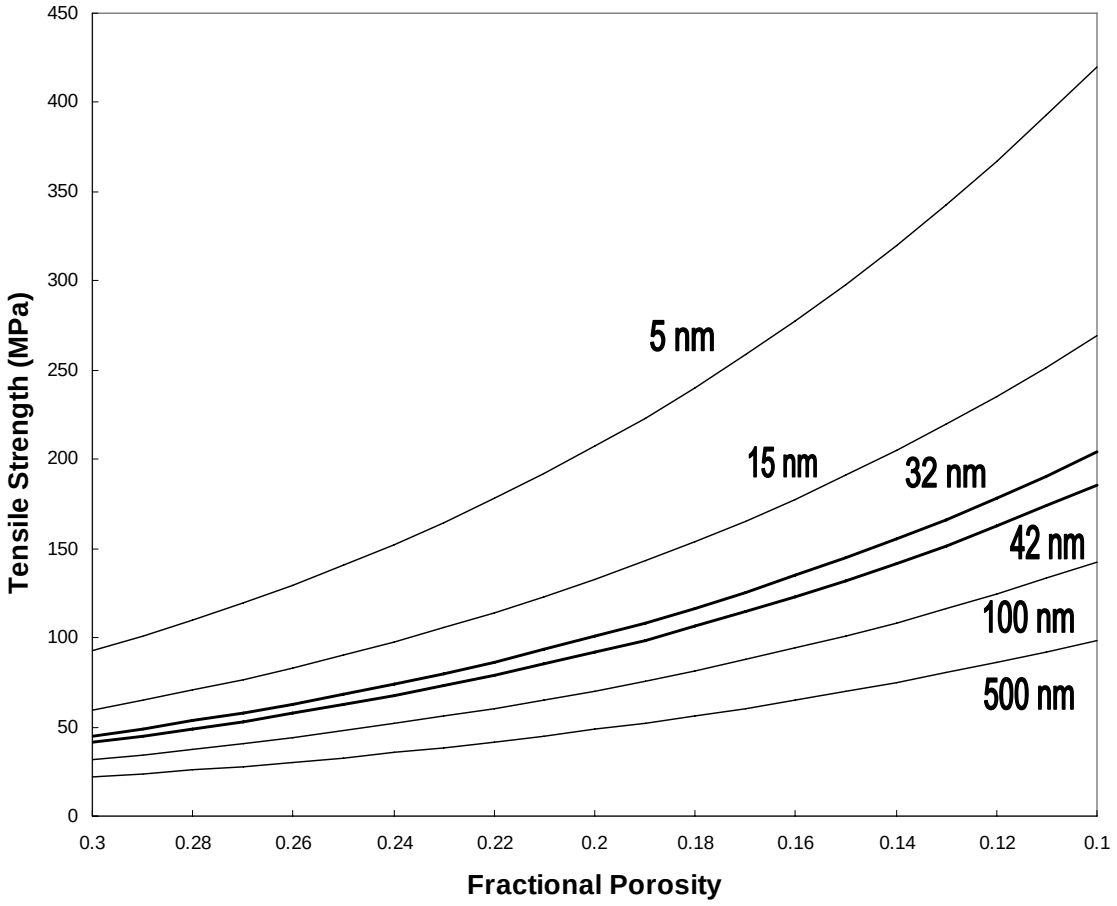

Figure 40. Prediction of tensile strength of nanostructured Ag based on grain size and porosity. The 32 and 42 nm grain sizes correspond to the grain sizes associated with our processing temperatures.

In this plot, an n value of 6 was chosen for Eq. (4). This fits the actual strength data remarkably well – square samples processed at 125°C (corresponding to serpentine

samples with a grain size of 32 nm and a porosity of 0.27) exhibited strengths of approximately 55 MPa, as compared to a predicted value of 58 MPa. Square samples processed at higher temperatures (corresponding to serpentine samples with a grain size of 42 nm and a porosity of 0.17) exhibited strengths of approximately 93 MPa, as compared to a predicted value of 114 MPa. A high value of n has been attributed to pores with cusps at their corners. Compared to spherical pores, such cusp-shaped pores would be expected to result in lower strengths, since the cusps can act as crack initiation sites for fracture. Thus, the fact that a large value of n was used to fit our data may suggest that the pores had a non-spherical shape. If this is the case, increasing the processing temperatures would be expected to improve strength since pore rounding would be expected at higher temperatures.

The tensile strength of fully dense, recrystallized Ag is approximately 142 MPa.[21] If we use the Hall-Petch relationship and Qin's data to calculate the grain size, this corresponds to a 4 μm grain size.[41] As discussed in Chapter 2, decreasing the grain size increases strength, so that fully dense Ag with a 32 nm grain size would have a tensile strength of approximately 380 MPa. This represents the maximum strength that could be achieved if a sample could be fully densified, while retaining this grain size.

If a Ag sample with a grain size of 32 nm could be fully densified, the strength could be improved by a factor of approximately 6 compared to the strengths of the samples achieved through processing in this work. If the grain size was maintained at 6 nm throughout the processing of a Ag sample, the strength would only be expected to improve by a factor of approximately 2.5 over a 32 nm sample of similar porosity. Therefore, the most effective way to further increase the strength of a sample would be to

densify the sample as much as possible. Higher processing temperatures would be expected to lead to more densification, so if strength needed to be increased for a particular application, the highest temperatures possible should be used, taking into consideration the temperature limitations and sensitivity of the sample for the desired application. It is also important to note that although reducing grain size would also strengthen the sample, it would come at a cost of reduced conductivity, so the ideal grain size would have to be optimized for both strength and conductivity for a particular application.

5.2 RESISTIVITY

The resistivity of our samples compared well with previous work involving the use of Ag NPs to create electrically conductive features. A summary of previous work with our results included is presented in Figure 41. Once again, pressure assisted samples are indicated by solid points, whereas outlined points indicate samples that were sintered without applied pressure.

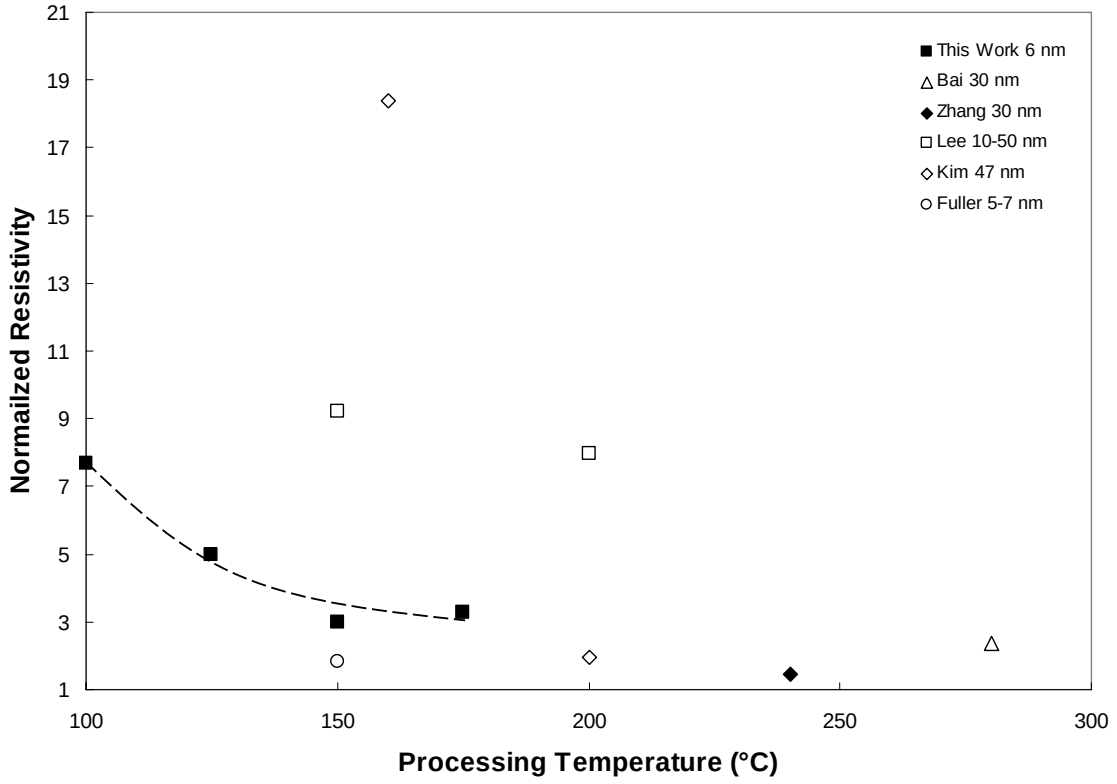

Figure 41. A plot of normalized resistivity vs. processing temperature for previous work utilizing Ag NPs. Solid points represent techniques involving pressure-assisted sintering, while outlined points represent samples prepared using only heating. Lee, Kim and Fuller utilized ink-jet printing, while Bai and Zhang utilized screen/stencil printing.[5,6,8,18,20]

Figure 41 shows that the low resistivities achieved by our samples at low processing temperatures are comparable to only one other set of reported data (Fuller), which also utilized smaller NPs than the other groups. These conductivities presented by Fuller et al. are far better than what other groups have been able to produce using similar processing techniques. By comparing the conductivities and particle size reported by Fuller et al. to Qin's model, we are able to determine the apparent density of their deposits. According to Qin's data, the conductivities reported by Fuller et al. require a minimum grain size of 25 nm for a fully dense material. However, the densities reported by other researchers using processing techniques similar to Fuller are typically around 80%. The grain size required to achieve Fuller et al.'s reported conductivities assuming that their samples were 80% dense is calculated to be 89 nm. In our experiments, grain coarsening resulted in grain sizes of less than 50 nm, and our silver nanoparticles were processed in the absence of organic capping agents which have been shown to hinder coarsening. Thus, there appears to be an inconsistency in the conductivity measurements reported by Fuller et al. since neither full densification nor grain growth to 89 nm are consistent with the 150°C processing temperature utilized by Fuller et al. Comparing the other data to our current results, we see that the LAMA process is capable of achieving the lowest resistivities at low processing temperatures.

The fracture surface shown in Figure 12 shows the columnar growth associated with the deposition of Ag using the LAMA process. This fracture surface appears to show significant columnar porosity. Note however, that as a fracture surface, the appearance of columnar porosity may be an artifact of intercolumnar fracture rather than

porosity. If the macroscopic columnar porosity was inherent to the sample, it would be expected to prevent conductivities of the values measured in this work. Figure 42 shows a low magnification SEM image of a cross-section of a sample after tension testing.

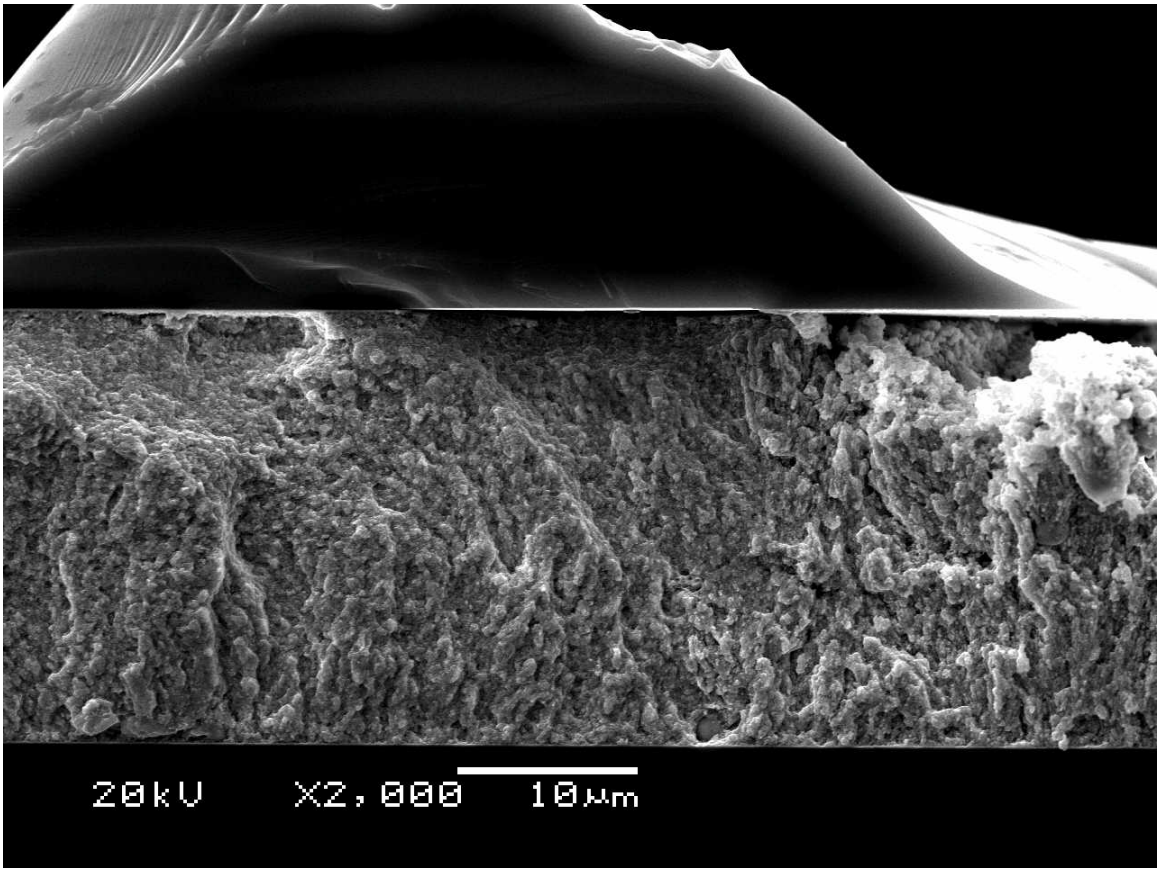

Figure 42. SEM image of a cross-section of a sample after tension testing. The smooth region at the top of the sample is Si removed from the upper substrate during fracture. The granular region is the Ag deposit.

Figure 43 is a higher magnification SEM image of the same region shown in Figure 42, showing the morphology of the Ag deposit in greater detail.

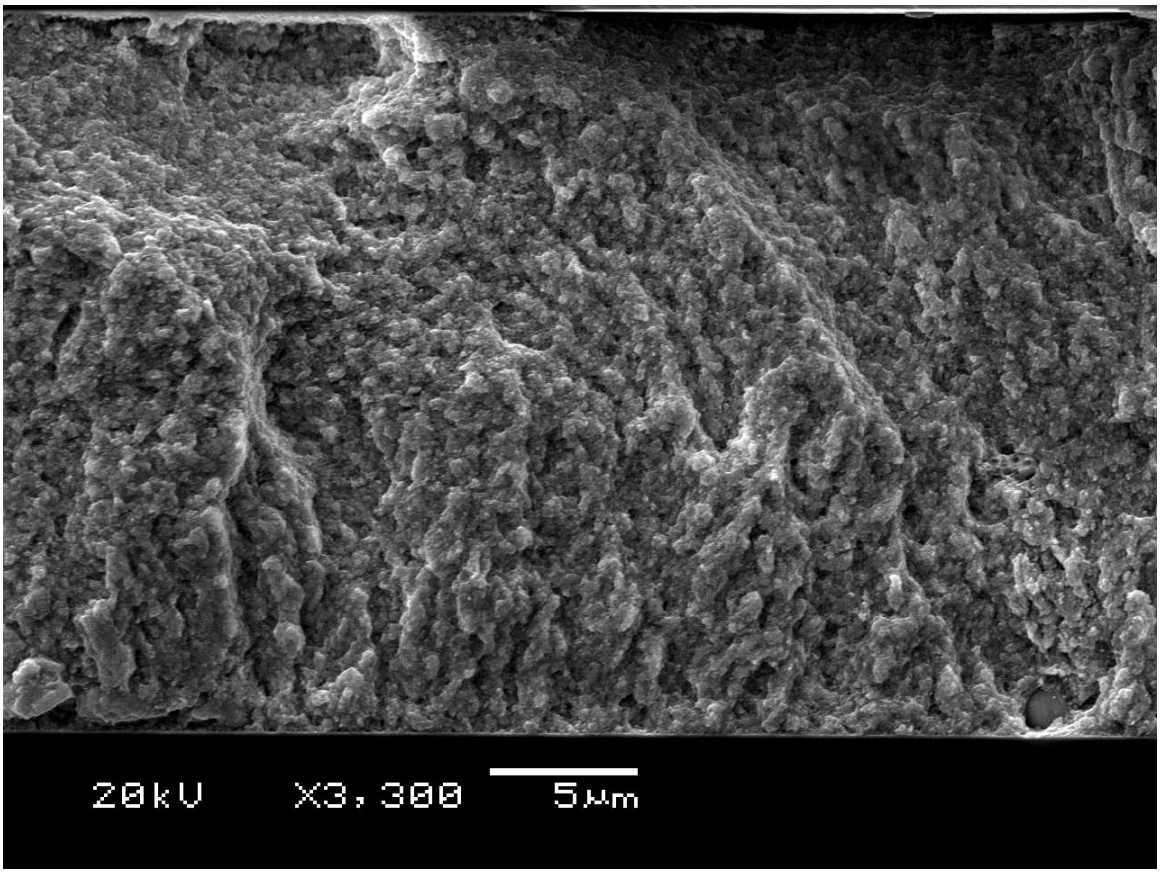

Figure 43. Higher magnification SEM image of the Ag deposit from Figure 42.

The expected intercolumnar fracture of the surface shown in Figures 42 and 43 makes identification of the dominant pore shape difficult, but these images along with the conductivities of the samples imply that most of the porosity is on the nanoscale and not macroscopic columnar porosity.

Both densification and a small amount of grain growth would further improve the conductivities of our samples. If a 32 nm Ag sample were fully densified, it would have a normalized resistivity of 1.5, an improvement in conductivity of about a factor of 3.

The electron mean free path in our samples is still limited by grain size. An increase in grain size to 47 nm would result in a sample with the same electron mean free path as bulk Ag with a grain size of several microns, and therefore improve conductivity (while decreasing strength). Increasing the grain size from 32 nm (maintaining 80% density) to 100 nm would result in a factor of 3 increase in conductivity. If desirable, both density and grain size could be increased by increasing the processing temperature of the sample.

5.3 DENSIFICATION

A hot-pressing model based on analysis by Coble (Eq. (8)) was assessed to determine its validity to our experimental results. This model was a final stage sintering model and assumed that grain boundary diffusion was the dominant sintering mechanism. Because there is a paucity of data for grain boundary diffusion for Ag nanomaterials at low temperatures, it was assumed that the grain boundary diffusion coefficient could be extrapolated to our conditions. It was also assumed that grain boundary thickness was not different for a nanostructured material, which is justified by the work of Siegel and Thomas.[59]

The influence of fractional density on the densification rate is shown in Figure 44.[60]

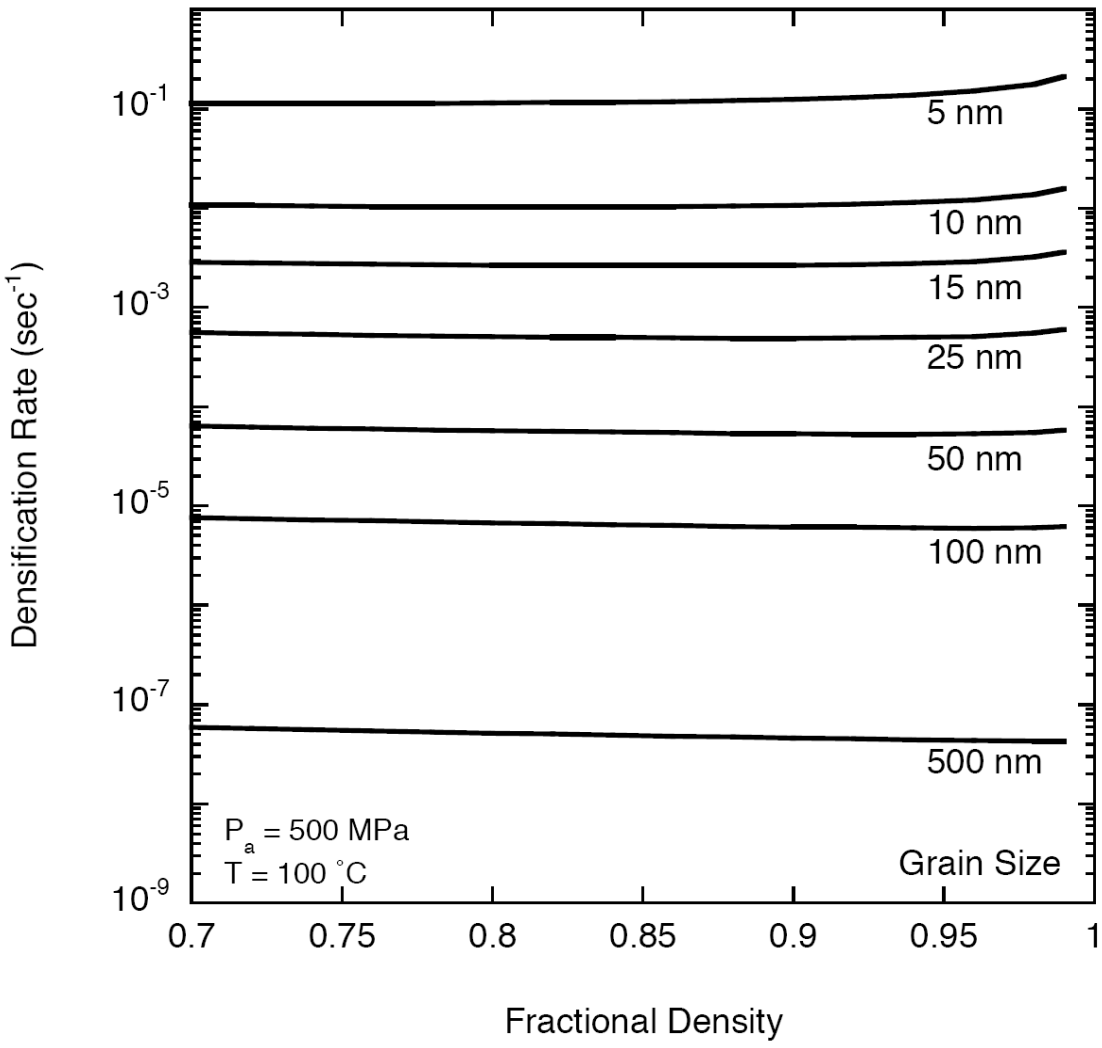

Figure 44. The effect of fractional density on densification rate.[60]

Figure 45 shows the effect of surface energy on densification rate.

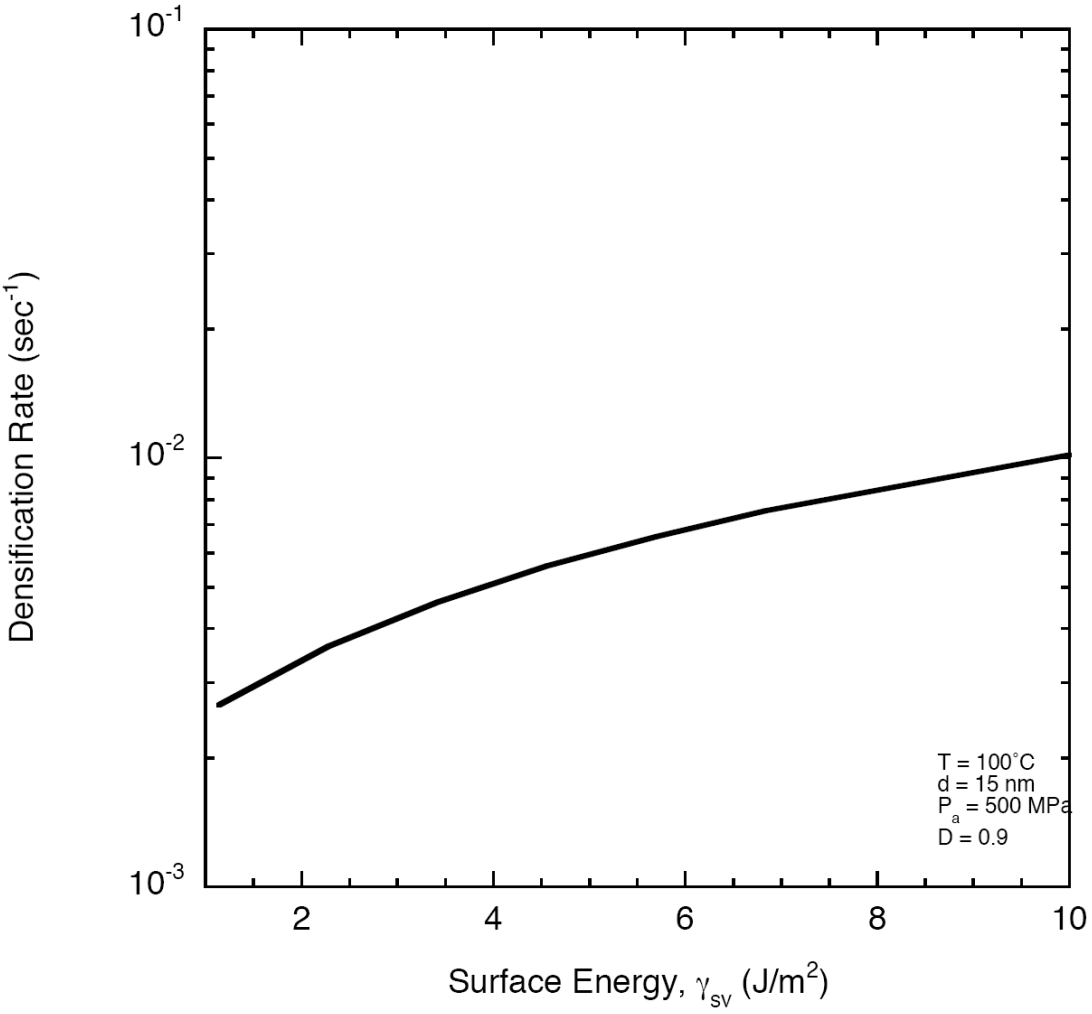

Figure 45. The effect of surface energy on densification rate.[60]

From Figure 44 it is apparent that fractional density does not have a significant effect on the densification rate. The surface energy has a modest effect on densification rate (Figure 45).

Figure 46 shows the effect of pressure on densification rate for different grain sizes at a temperature of 100°C.

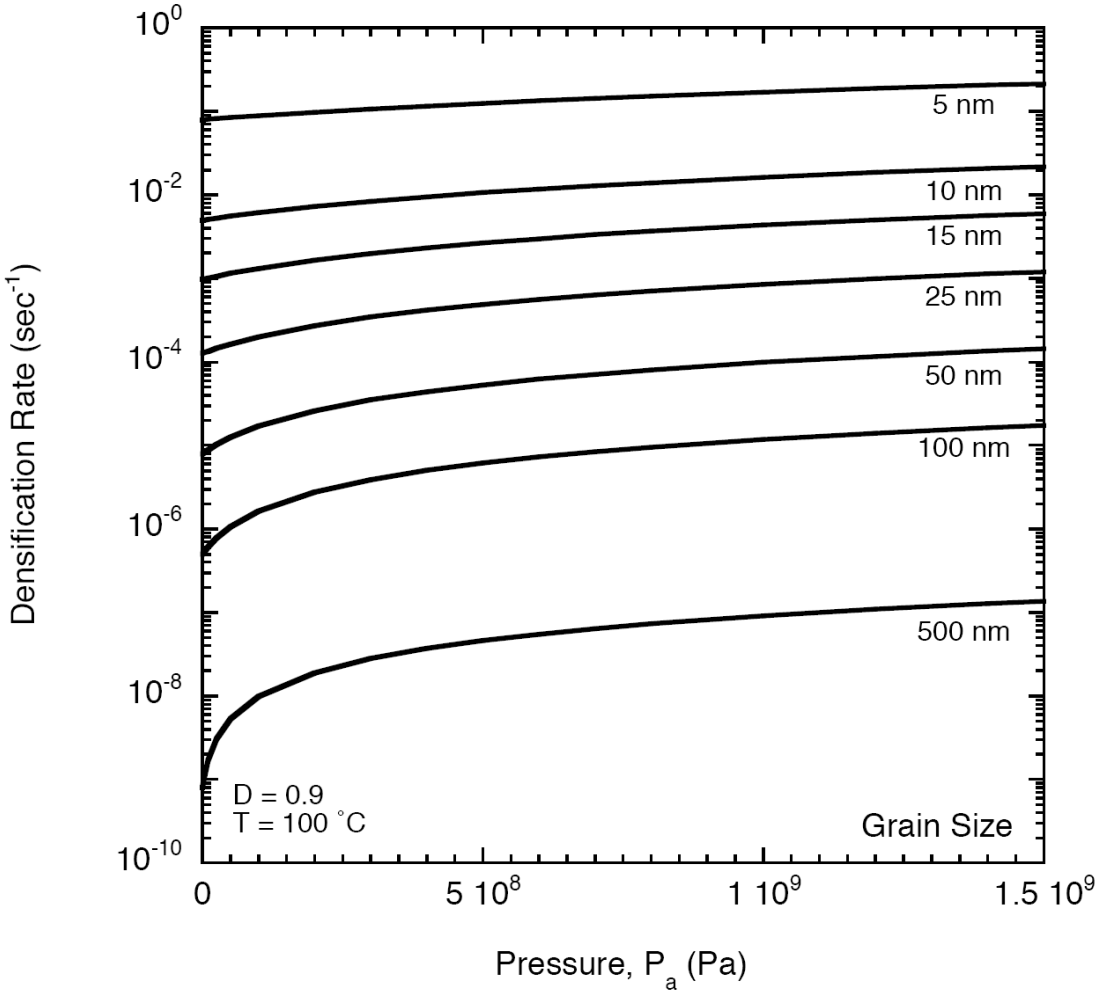

Figure 46. The effect of pressure on Ag densification rate for different grain sizes, for an initial density of 0.9 and at a temperature of 100°C.[60]

Figure 46 indicates that at as grain size decreases, changing pressure has a smaller effect on overall densification rate. This was consistent with our experimental findings, in

which our samples had very fine grains and the densification rate appeared to be insensitive to the amount of pressure applied during processing. Note also that conventional hot pressing is typically performed at modest pressures (30 MPa) on sub-micron grains where the influence of pressure on densification rate is much stronger.

Figure 47 shows that temperature has a strong effect on densification rate, even at the low temperatures involved in this study. Note that the densification rate for 25 nm grains is two orders of magnitude higher than the densification rate for 100 nm grains under otherwise identical conditions. The strong effect of temperature on density was also supported by our experimental results.

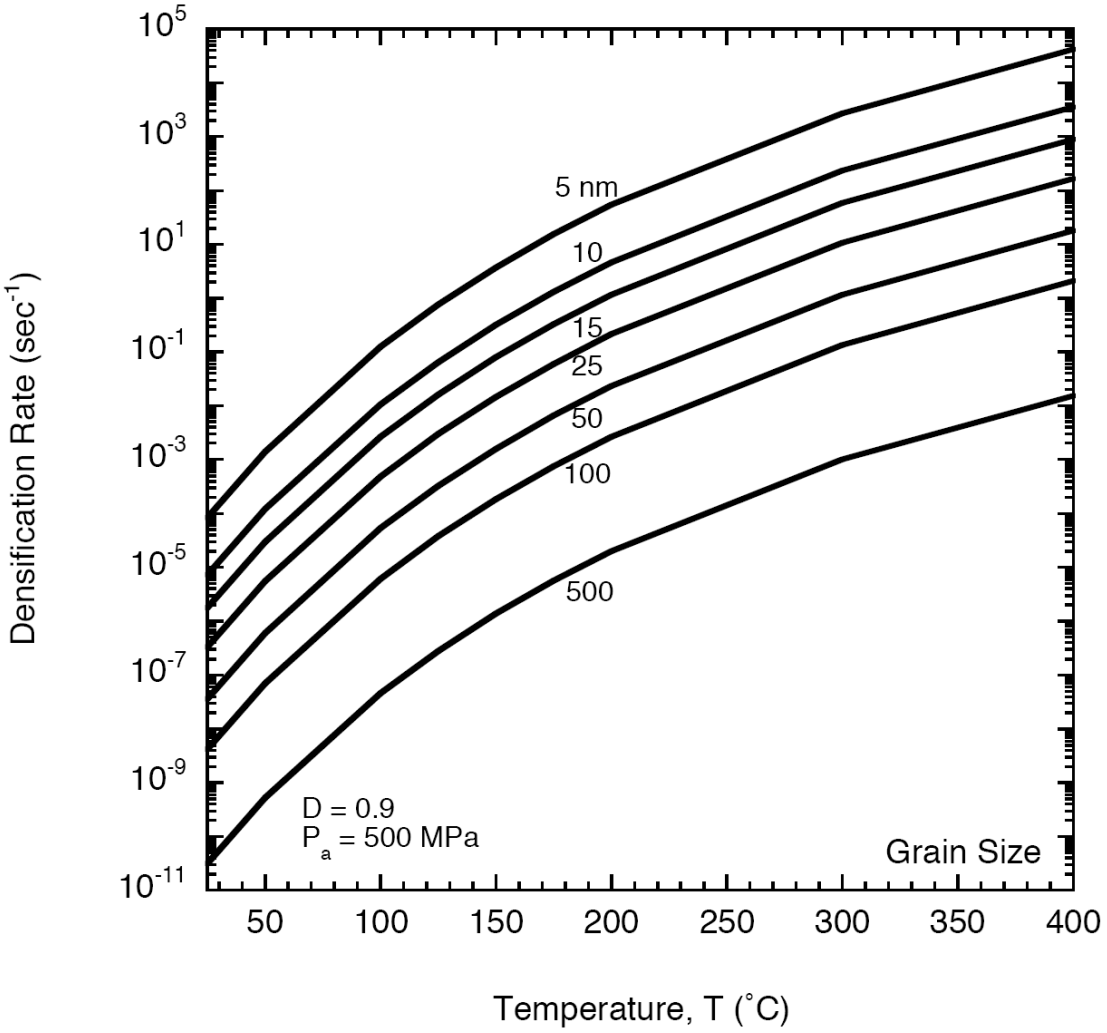

Figure 47. The effect of temperature on Ag densification rate for different grain sizes, at an initial density of 0.9 and a pressure of 500 MPa.[60]

Given that pressure did not have an apparent effect on the densification rate of our samples (See Figure 37), we can consider a pressureless sintering model to determine the predicted relative rates of coarsening and densification in our samples. As discussed in

Chapter 2, the dimensionless parameter Γ from Eq. (7) is a direct measure of the rates of coarsening and densification. We computed Γ as a function of temperature and compared the predictions of this model to our experimental results. For clarity, Figure 48 is presented as log (Γ) vs temperature.

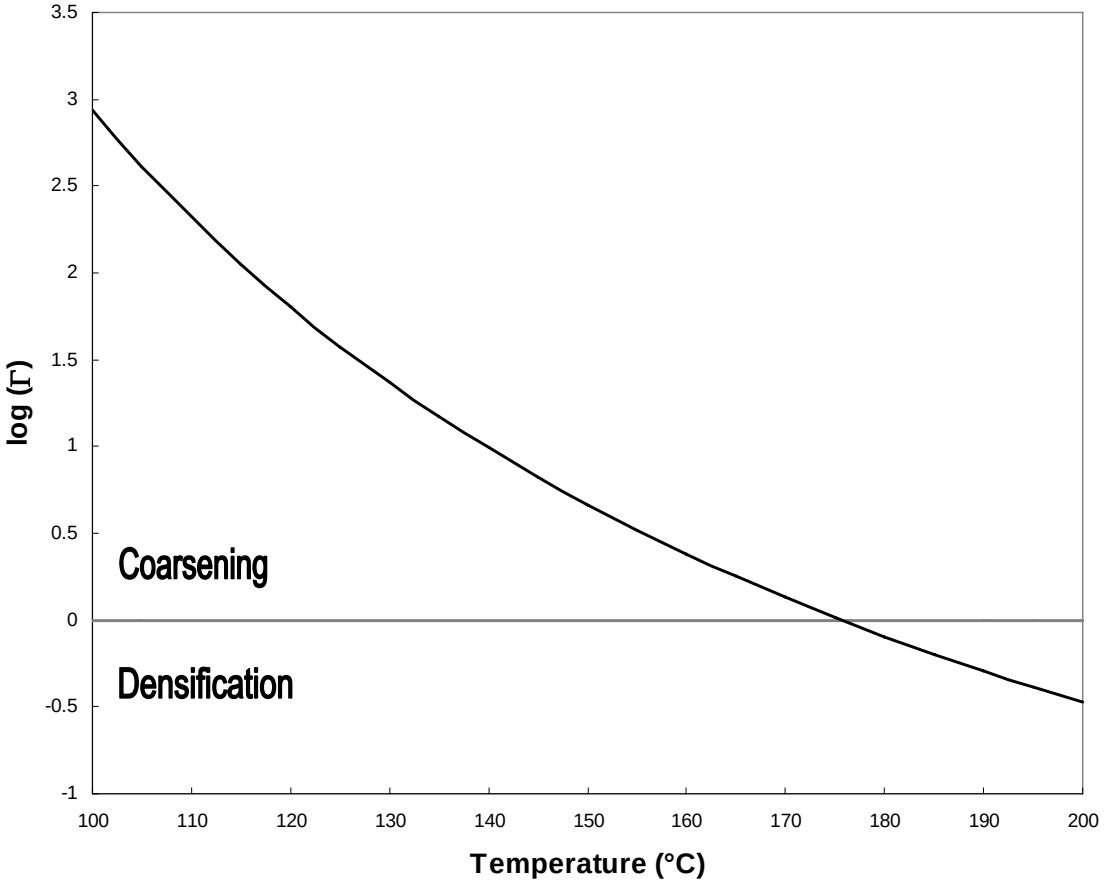

Figure 48. log (Γ) as a function of temperature for Ag.

For this analysis, the same values of material properties of nanostructured Ag at low temperatures were used as those used for the hot pressing model discussed

previously. Figure 48 shows an expected transition from predominantly coarsening to predominantly densification at approximately 175°C when log (Γ) < 0. Our samples were processed at temperatures of 100 - 175°C, and exhibited both densification and coarsening, even in the absence of pressure. This behavior agrees qualitatively with processing near a transitional temperature, as predicted by theory.

Based on our experimental results, as well as this analysis, it seems clear that the further densification of our samples would be most easily achieved by increasing the processing temperature. Even a modest increase to 200°C from 175°C would be expected to increase the densification rate by nearly an order of magnitude. For samples of our grain size, increasing the pressure is not an effective method for increasing densification rate by diffusional processes (see Figure 46). Since densification would improve both strength and conductivity, the properties of samples would be improved by increasing the densification rate. The ideal processing temperature would therefore be the highest temperature allowed, given the temperature constraints associated with the desired application.

Previous experiments on LAMA-produced Ag films that were annealed showed that samples that were annealed in the absence of pressure did not densify. Instead, these samples coarsened at annealing temperatures up to 400°C. It was postulated that the relatively slow heating rate used in those experiments (5-25°C/min) promoted coarsening during heating and that this resulted in an increase in the coarsening-to-densification transition temperature. If this is the case, a faster heating rate should lower the transition temperature and possibly densify samples without pressure. In this work, the samples reached the processing temperature very quickly (usually reaching within 2°C of the

processing temperature in less than a minute, a heating rate of greater than 100°C/min). The fact that the samples in this study showed densification at low processing temperatures without pressure, confirmed that rapid heating can be used to induce densification in nanostructured metals, even in the absence of pressure.

Chapter 6: *Conclusions and Future Work*

6.1 CONCLUSIONS

This work showed that the LAMA process combined with low temperature post-processing can be used to produce high strength bonds from nanostructured silver. The strengths of our bonded samples exceeded 100 MPa at the processing temperature of 175°C. These strengths are similar to the strengths of bonded nanostructured Ag achieved previously, but at processing temperatures that were 50-100˚C lower. It was suggested that the reason for the lower processing temperatures was that, unlike chemically produced NPs that were studied previously, the LAMA process utilizes bare NPs that are not capped with organics that interfere with coarsening and densification. It was suggested that further improvements in strength could be most readily achieved by increasing density, although limiting grain growth during processing would also improve strength somewhat.

Electrical conductivity measurements on our samples following post-processing showed that the processing temperatures required to achieve high conductivities were lower than that achieved using most other direct-write methods. At post-processing temperatures of 150 and 175°C, our samples had conductivities approaching 33% of bulk polycrystalline Ag with micron-sized grains. These conductivities could be further increased by either increasing the density or the grain size of the samples.

Comparing our experimental results with existing pressureless and pressure-assisted densification models showed that our results agree qualitatively with theory. Our

experimental results were consistent with theory which predicted that pressure has a minimal effect on densification for ultra-fine grain samples such as ours. Increasing the processing temperature had a significant effect on the densification of the samples, again agreeing with theory. To achieve higher densities, higher processing temperatures would be required, although significant increases in densification rate are expected at temperatures as low as 200°C. Increasing the pressure during densification is not expected to significantly affect densification rate.

A final stage, pressureless sintering model predicts a transition from coarsening to densification at a temperature of 175°C, which also qualitatively agrees with the behavior of our samples, which exhibited both coarsening and densification in the temperature range of 100-175˚C. These results are different than those reported previously for pressureless sintered Ag processed at temperatures of 100-400˚C where minimal densification was reported. It was postulated that the faster heating rates used in this study (100˚C/min versus 5-25˚C/min used previously) may have contributed to increased densification because prolonged exposure to low temperatures during slow heating is expected to increase the coarsening-to-densification transition temperature. These results suggest that since both strength and conductivity improve with higher densities, the processing temperature should be the highest temperature allowed, given the temperature constraints for the particular application of the sample. Comparison with previous work shows the necessity of rapid heating to processing temperatures to limit coarsening and promote densification.

6.2. FUTURE WORK

A significant hurdle in the current LAMA process involves the feeding of the microparticle aerosol. The diameter of the deposition nozzle is limited by pumping capacity; the current system cannot maintain the desired vacuum level during deposition if the nozzle diameter is increased. Decreasing the pressure differential between the ablation and deposition chambers is not desirable since it can result in lower impaction velocities and films with lower densities. The feed rate of the microparticles is in turn limited by the size of the nozzle since the deposition nozzle tends to clog if the feeding rates are increased. Increasing the powder feeding rate is desirable, because the feeder operates more consistently at higher feed rates. Thus, acquiring higher capacity pumps would enable higher powder feed rates, and lead to more consistent deposition. A more consistent deposition would improve the quality of the deposits and simplify the analysis of experiments due to the deposition thickness fluctuations that result from the current feeder design.

In terms of sample analysis, the non-uniformity in the density of the deposits is not well understood. A better of understanding of this non-uniformity in the as-deposited lines and well as how these density gradients evolve during sintering would be helpful in identifying routes to achieving higher densities. TEM analysis of cross-sections of the deposited lines before and after compression and after annealing would be illuminating in terms of both defect analysis and the densification process.

Analysis of the fracture process in bonded samples would be beneficial in multiple ways. It would be instructive to be able to compare the crack propagation energy for samples under differing processing conditions. Understanding where failure

of the sample initiates could also be helpful in terms of strengthening the samples further. Analysis of the mechanism of bonding between the Ag and the blank top metallized substrate could also lead to ideas on how to improve strength at the Ag-Au interface.

References

(1) Castro, T.; Reifenberger, R.; Choi, E.; Andres, R. P. Size-dependent melting temperature of individual nanometer-sized metallic clusters *Physical Review B (Condensed Matter)* **1990**, *42*, 8548-56.

(2) Olynick, D. L.; Gibson, J. M.; Averback, R. S. In *Materials Science & Engineering A (Structural Materials: Properties, Microstructure and Processing)*; Elsevier Office of Naval Res.: Switzerland, 1995; Vol. A204; pp 54-58.

(3) Yeadon, M.; Yang, J. C.; Averback, R. S.; Bullard, J. W.; Gibson, J. M. In *Nanostructured Materials*; Elsevier: USA, 1998; Vol. 10; pp 731-739.

(4) Park, J.-W.; Baek, S.-G. Thermal behavior of direct-printed lines of silver nanoparticles *Scripta Materialia* **2006**, *55*, 1139-1142.

(5) Kim, D.; Moon, J. Highly conductive ink jet printed films of nanosilver particles for printable electronics *Electrochemical and Solid-State Letters* **2005**, *8*, 30-33.

(6) Lee, H.-H.; Chou, K.-S.; Huang, K.-C. Inkjet printing of nanosized silver colloids *Nanotechnology* **2005**, *16*, 2436-2441.

(7) Moon, K.-S.; Dong, H.; Maric, R.; Pothukuchi, S.; Hunt, A.; Li, Y.; Wong, C. P. Thermal behavior of silver nanoparticles for low-temperature interconnect applications *Journal of Electronic Materials* **2005**, *34*, 168-175.

(8) Fuller, S. B.; Wilhelm, E. J.; Jacobson, J. M. Ink-jet printed nanoparticle microelectromechanical systems *Journal of Microelectromechanical Systems* **2002**, *11*, 54-60.

(9) Rane, S.; Puri, V.; Amalnerkar, D. A study on sintering and microstructure development of fritless silver thick film conductors *Journal of Materials Science: Materials in Electronics* **2000**, *11*, 667-674.

(10) Bai, J. G.; Zhang, Z. Z.; Calata, J. N.; Lu, G.-Q. Low-temperature sintered nanoscale silver as a novel semiconductor device-Metallized Substrate interconnect material *IEEE Transactions on Components and Packaging Technologies* **2006**, *29*, 589-593.

(11) Chung, J.; Ko, S.; Bieri, N. R.; Grigoropoulos, C. P.; Poulikakos, D. Conductor microstructures by laser curing of printed gold nanoparticle ink *Applied Physics Letters* **2004**, *84*, 801-803.

(12) Chung, J.; Bieri, N. R.; Ko, S.; Grigoropoulos, C. P.; Poulikakos, D. In-tandem deposition and sintering of printed gold nanoparticle inks induced by continuous Gaussian laser irradiation *Laser Ablation Applied Physics A: Materials Science and Processing* **2004**, *79*, 1259-1261.

(13) Chung, J.; Ko, S.; Grigoropoulos, C. P.; Bieri, N. R.; Dockendorf, C.; Poulikakos, D. Damage-free low temperature pulsed laser printing of gold nanoinks on polymers *Journal of Heat Transfer* **2005**, *127*, 724-732.

(14) Chung, J.; Ko, S.; Grigoropoulos, C. P.; Bieri, N. R.; Dockendorf, C.; Poulikakos, D. In *Proceedings of the ASME Heat Transfer/Fluids Engineering Summer Conference 2004, HT/FED 2004, Jul 11-15 2004*; American Society of Mechanical

Engineers, New York, NY 10016-5990, United States: Charlotte, NC, United States, 2004; Vol. 4; pp 597-605.

(15) Bieri, N. R.; Chung, J.; Haferl, S. E.; Poulikakos, D.; Grigoropoulos, C. P. Microstructuring by printing and laser curing of nanoparticle solutions *Applied Physics Letters* **2003**, *82*, 3529-3531.

(16) Schwarzbauer, H.; Kuhnert, R. Novel large area joining technique for improved power device performance *IEEE Transactions on Industry Applications* **1991**, *27*, 93-95.

(17) Zhang, Z.; Calata, J. N.; Bai, J. G.; Lu, G.-Q. In *MPMD Fifth Global Innovations Proceedings, Surfaces and Interfaces in Nanostructured Materials and Trends in LIGA, Miniaturization, and Nanoscale Materials, Mar 14-18 2004*; Minerals, Metals and Materials Society, Warrendale, United States: Charlotte, NC., United States, 2004; pp 129-135.

(18) Zhang, Z.; Lu, G.-Q. Pressure-assisted low-temperature sintering of silver paste as an alternative die-attach solution to solder reflow *IEEE Transactions on Electronics Packaging Manufacturing* **2002**, *25*, 279-283.

(19) Ukita, Y.; Tateyama, K.; Segawa, M.; Tojo, Y.; Gotoh, H.; Oosako, K. Lead free die mount adhesive using silver nanoparticles applied to power discrete package *Advancing Microelectronics* **2005**, *32*, 8-11.

(20) Bai, J. G.; Calata, J. N.; Zhang, Z. Z.; Lu, G.-Q. In *2005 ASME International Mechanical Engineering Congress and Exposition, IMECE, Nov 5-11 2005*; American Society of Mechanical Engineers, New York, NY 10016-5990, United States: Orlando, FL, United States, 2005; Vol. 5; pp 415-424.

(21) Buch, A. *Pure Metals Properties: A Scientific-Technical Handbook*; ASM International and Freund Publishing House Ltd: Materials Park, 1999.

(22) Rahaman, M. N. *Ceramic Processing and Sintering*; 2nd ed.; Marcel Dekker, Inc.: New York, 2003.

(23) Hayashi, C.; Kashu, S.; Oda, M.; Naruse, F. Use of nanoparticles as coatings *12th International Vacuum Congress, Oct 12-16 1992 Materials Science & Engineering A: Structural Materials: Properties, Microstructure and Processing* **1993**, *A163*, 157-161.

(24) Kashu, S.; Fuchita, E.; Manabe, T.; Hayashi, C. Deposition Of Ultra Fine Particles Using a Gas Jet *Japanese Journal of Applied Physics, Part 2: Letters* **1984**, *23*, 910-912.

(25) Oda, M.; Fuchita, E.; Tsuneizumi, M.; Kashu, S.; Hayashi, C. Gas deposition films of ultra fine particles *Nanostructured Materials* **1992**, *1*, 203-206.

(26) Oda, M.; Katsu, I.; Tsuneizumi, M.; Fuchita, E.; Kashu, S.; Hayashi, C. In *Proceedings of the Symposium on Nanophase and Nanocomposite Materials, Dec 1-3 1992*; Publ by Materials Research Society, Pittsburgh, PA, USA: Boston, MA, USA, 1993; Vol. 286; pp 121-130.

(27) Nichols, W. T.; Keto, J. W.; Henneke, D. E.; Brock, J. R.; Malyavanatham, G.; Becker, M. F.; Glicksman, H. D. Large-scale production of nanocrystals by laser ablation of microparticles in a flowing aerosol *Applied Physics Letters* **2001**, *78*, 1128-1130.

(28) Nichols, W. T.; Malyavanatham, G.; Beam, M. P.; Henneke, D. E.; Brock, J. R.; Becker, M. F.; Keto, J. W. Synthesis of nanostructured WC films by supersonic impaction of nanoparticle aerosols *Materials Research Society Symposium - Proceedings The 1999 MRS Fall Meeting - Symposium F 'Nanophase and Nanocomposite Materials III', Nov 29-Dec 2 1999* **2000**, *581*, 193-198.

(29) Nichols, W. T.; Malyavanatham, G.; Henneke, D. E.; Brock, J. R.; Becker, M. F.; Keto, J. W.; Glicksman, H. D. Gas and Pressure Dependence for the Mean Size of Nanoparticles Produced by Laser Ablation of Flowing Aerosols *Journal of Nanoparticle Research* **2000**, *2*, 141-145.

(30) Nichols, W. T.; O'Brien, D. T.; Malyavanatham, G.; Becker, M. F.; Keto, J. W. In *Nanophase and Nanocomposite Materials IV, Nov 26-29 2001*; Materials Research Society: Boston, MA, United States, 2002; Vol. 703; pp 209-214.

(31) Becker, M. F.; Brock, J. R.; Cai, H.; Henneke, D.; Hilsz, L.; Keto, J. W.; Lee, J.; Nichols, W. T.; Glicksman, H. D. In *Proceedings of the 1998 Conference on Lasers and Electro-Optics, CLEO, May 3-8 1998*; IEEE, Piscataway, NJ, USA: San Francisco, CA, USA, 1998; pp 151-152.

(32) Becker, M. F.; Brock, J. R.; Cai, H.; Henneke, D. E.; Keto, J. W.; Lee, J.; Nichols, W. T.; Glicksman, H. D. Metal nanoparticles generated by laser ablation *Nanostructured Materials Proceedings of the 1998 TMS Annual Meeting & Exposition, Feb 15-19 1998* **1998**, *10*, 853-863.

(33) A.D. Albert; Huang, C.; Becker, M. F.; Keto, J. W.; Kovar, D. Deposition of Nanostructured Silver Lines and Films from Aerosols Produced by LAMA *Proceedings of the International Symposium on Synergistic Effects of Materials and Processing,* **2006**, *JSME No. 06-207*, 1-6.

(34) Huang, C.; Nichols, W. T.; O'Brien, D. T.; Becker, M. F.; Keto, J. W.; Kovar, D. Supersonic Jet Deposition of Silver Nanoparticle Aerosols: Correlations of Impact Conditions and Film Morphologies *J. Appl. Phys* **2007**, *In Press*.

(35) Hall, E. O. The deformation and aging of mild steel *Proceedings of the Physical Society of London* **1951**, *B64*.

(36) Petch, N. J. The cleavage strength of polycrystals *Journal of the Iron Steel Institute* **1953**, *25*.

(37) Johnson, K. L. *Contact Mechanics*; Cambridge Univeristy Press: Cambridge, 1985.

(38) Koch, C. C.; Narayan, J. The Inverse Hall-Petch Effect: Fact or Artifact? *Mat. Res. Soc. Symp.* **2001**, *B5.1.1*.

(39) Weertman, J. R. In *Nanostructured Materials*; Koch, C., Ed.; Noyes Publications: Norwich, 2002; pp 393-417.

(40) Song, H. W.; Guo, S. R.; Hu, Z. Q. A coherent polycrystal model for the inverse Hall-Petch relation in nanocrystalline materials *Nanostructured Materials* **1999**, *11*, 203-210.

(41) Qin, X. Y.; Wu, X. J.; Zhang, L. D. Microhardness of nanocrystalline silver *Nanostructured Materials* **1995**, *5*, 101-110.

(42) Thummler, F.; Oberacker, R. *Introduction to Powder Metallurgy*; The Institue of Materials: London, 1993.

(43) Mandal, S. K.; Gangopadhyay, A.; Chaudhuri, S.; Pal, A. K. Electron transport process in discontinuous silver film *Vacuum* **1999**, *52*, 485-490.

(44) Huang, C.; Becker, M. F.; Keto, J. W.; Kovar, D. Annealing of Nanostructured Silver Films Produced by Supersonic Deposition of Nanoparticles *J. Appl. Phys* **2007**, *In Press*.

(45) Huang, C. Dissertation, University of Texas at Austin, 2006.

(46) Qin, X. Y.; Zhang, W.; Zhang, L. D.; Jiang, L. D.; Liu, X. J.; Jin, D. Low-temperature resistance and its temperature dependence in nanostructured silver *Physical Review B (Condensed Matter)* **1997**, *56*, 10596-10604.

(47) Reiss, G.; Vancea, J.; Hoffmann, H. Grain-Boundary Resistance in Polycrystalline Metals *Phys. Rev. Lett.* **1986**, *56*, 2100 LP - 2103.

(48) Schaefer, H.-E.; Würschum, R.; Birringer, R.; Gleiter, H. Structure of nanometer-sized polycrystalline iron investigated by positron lifetime spectroscopy *Phys. Rev. B J1 - PRB* **1988**, *38*, 9545 LP - 9554.

(49) Yan, M. F. Microstructural control in the processing of electronic ceramics *Mat. Sci. Eng.* **1981**, *48*, 53-72.

(50) Shewmon, P. *Diffusion in Solids*; 2nd ed.; TMS: Warrendale, PA, 1989.

(51) Guy, A. G. *Introduction to Materials Science*; 1st ed.; McGraw-Hill Book Co.: New York, 1972.

(52) Inman, M. C.; Tipler, H. R. Interfacial energy and composition in metals and alloys *Metall. Rev.* **1963**, *8*.

(53) McClean, D. M. *Grain Boundaries in Metals*; Oxford Univeristy Press: Oxford, 1957.

(54) Richerson, D. W. *Modern Ceramic Engineering: Properties, Processing, and Use in Design*; 2nd ed.; Marcel Dekker, Inc.: New York, 1992.

(55) Coble, R. L. Diffusion models for hot-pressing with surface energy and pressure effects as driving forces *J. Appl. Phys* **1970**, *41*, 4798-4807.

(56) Hammond, C. *The Basics of Crystallography and Diffraction*; Oxford Univeristy Press: Oxford, 1997.

(57) Williamson, G. K.; Hall, W. H. X-ray line broadening from filed aluminium and wolfram *Acta Metall.* **1953**, *1*.

(58) Moffatt, W. G.; Wulff, J. Strength of silver brazed joints in mild steel *J. Met.* **1957**, 442-445.

(59) Siegel, R. W.; Thomas, G. J. Grain boundaries in nanophase materials *Ultramicroscopy* **1992**, *40*, 376-384.

(60) Kovar, D.; Albert, A., Ed.: Austin, 2007.

Vita

André David Albert was born in Austin, Texas on July 5, 1979 and raised by his parents, Madeleine Albert and Joseph Graf. He attended high school at the Science Academy of Austin at Lyndon Baines Johnson. He received three degrees from the University of Texas at Austin, a B.S. in Mechanical Engineering in 2001 (with Honors), an M.S.E. in Materials Science and Engineering in 2003 and a Ph.D. in Materials Science in Engineering in 2007. He is happily married to Sara Rose Albert and currently resides in Austin, Texas.

Permanent address: 206 W. 38th #102, Austin, Texas 78705

This dissertation was typed by the author.